

Article

Asymmetric Dinuclear Lanthanide(III) Complexes from the Use of a Ligand Derived from 2-Acetylpyridine and Picolinoylhydrazide: Synthetic, Structural and Magnetic Studies †

Diamantoula Maniaki ¹, Panagiota S. Perlepe ^{2,3}, Evangelos Pilichos ¹, Sotirios Christodoulou ⁴, Mathieu Rouziers ², Pierre Dechambenoit ^{2,*}, Rodolphe Clérac ^{2,*}  and Spyros P. Perlepes ^{1,5,*}

¹ Department of Chemistry, University of Patras, 26504 Patras, Greece; dia.maniaki@gmail.com (D.M.); pilvag@gmail.com (E.P.)

² CNRS, Univ. Bordeaux, CNRS, Centre de Recherche Paul Pascal, UMR 5031, 33600 Pessac, France; panagiota.perlepe@crpp.cnrs.fr (P.S.P.); mathieu.rouziers@crpp.cnrs.fr (M.R.)

³ CNRS, Univ. Bordeaux, Bordeaux INP, ICMCB, UMR 5026, 33600 Pessac, France

⁴ ICFO-Institut de Ciències Fòtoniques, The Barcelona Institute of Nanoscience and Nanotechnology, Castelldefels, 08860 Barcelona, Spain; Sotirios.Christodoulou@alumni.icfo.eu (S.C.)

⁵ Foundation for Research and Technology-Hellas (FORTH), Institute of Chemical Engineering Sciences (ICE-HT), Platani, P.O. Box 1414, 26504 Patras, Greece

* Correspondence: pierre.dechambenoit@crpp.cnrs.fr (P.D.); rodolphe.clerac@crpp.cnrs.fr (R.C.); perlepes@patreas.upatras.gr (S.P.P.); Tel.: +33-556845671 (P.D.); +33-556845650 (R.C.); +30-2610-996730 (S.P.P.)

† This article is dedicated to the memory of Professor Kyriakos Riganakos, an excellent academician, a great food chemistry scientist and a precious friend.

Academic Editor: Takashiro Akitsu

Received: 25 May 2020; Accepted: 5 July 2020; Published: 10 July 2020



Abstract: A family of four Ln(III) complexes has been synthesized with the general formula $[\text{Ln}_2(\text{NO}_3)_4(\text{L})_2(\text{S})]$ (Ln = Gd, Tb, Er, and S = H₂O; **1**, **2** and **4**, respectively/Ln = Dy, S = MeOH, complex **3**), where HL is the flexible ditopic ligand *N'*-(1-(pyridin-2-yl)ethylidene)pyridine-2-carbohydrazide. The structures of isostructural MeOH/H₂O solvates of these complexes were determined by single-crystal X-ray diffraction. The two Ln^{III} ions are doubly bridged by the deprotonated oxygen atoms of two “head-to-head” 2.21011 (Harris notation) L[−] ligands, forming a central, nearly rhombic {Ln^{III}₂(μ-OR)₂}⁴⁺ core. Two bidentate chelating nitrate groups complete a sphenocoronal 10-coordination at one metal ion, while two bidentate chelating nitrate groups and one solvent molecule (H₂O or MeOH) complete a spherical capped square antiprismatic 9-coordination at the other. The structures are critically compared with those of other, previously reported metal complexes of HL or L[−]. The IR spectra of **1–4** are discussed in terms of the coordination modes of the organic and inorganic ligands involved. The f-f transitions in the solid-state (diffuse reflectance) spectra of the Tb(III), Dy(III), and Er(III) complexes have been fully assigned in the UV/Vis and near-IR regions. Magnetic susceptibility studies in the 1.85–300 K range reveal the presence of weak, intramolecular Gd^{III}...Gd^{III} antiferromagnetic exchange interactions in **1** [$J/k_B = -0.020(6)$ K based on the spin Hamiltonian $\hat{H} = -2J(\hat{S}_{\text{Gd1}} \cdot \hat{S}_{\text{Gd2}})$] and probably weak antiferromagnetic Ln^{III}...Ln^{III} exchange interactions in **2–4**. Ac susceptibility measurements in zero dc field do not show frequency dependent out-of-phase signals, and this experimental fact is discussed for **3** in terms of the magnetic anisotropy axis for each Dy^{III} center and the oblate electron density of this metal ion. Complexes **3** and **4** are Single-Molecule Magnets (SMMs) and this behavior is optimally observed under external dc fields of 600 and 1000 Oe, respectively. The magnetization relaxation pathways are discussed and a satisfactory fit of the temperature and field dependencies of the relaxation time τ was achieved considering a model that employs Raman, direct, and Orbach relaxation mechanisms.

Keywords: asymmetric dinuclear lanthanide(III) complexes; dysprosium(III) and erbium(III) single-molecule magnets; magnetic properties; metal complexes of *N'*-(1-(1-pyridin-2-yl)ethylidene)pyridine-2-carbohydrazide; magnetization relaxation pathways; single-crystal X-ray structures

1. Introduction

Devices in the future, such as hard disks, will use components made from molecules instead of the traditional silicon-based electronics [1]. Molecules capable of retaining their magnetization in a given direction were discovered in the 1990s with the now famous $\{\text{Mn}^{\text{III}}_8\text{Mn}^{\text{IV}}_4\}$ acetate complex [2]. Such molecules (single-molecule magnets, SMMs) behave as tiny magnets at very low temperatures. The first generation of SMMs was based on transition-metal complexes [3,4]. Trivalent lanthanides, Ln(III)s, came into the scientific scene of the SMM area in 2003 with the mononuclear, double-decker complexes $[\text{Ln}^{\text{III}}(\text{pc})_2]^-$ (Ln = Tb, Dy; pc^{2-} = the phthalocyanine dianion) [5], and they are currently protagonists [6–34] in the interdisciplinary field of molecular magnetism. The latest scientific breakthrough was the synthesis of $[(\eta^5 - \text{cp}^*)\text{Dy}(\eta^5 - \text{cp}^{\text{iPr5}})][\text{B}(\text{C}_6\text{F}_5)_4]$, where cp^* is the pentamethylcyclopentadienyl(−1) group and cp^{iPr5} is the penta-iso-propylcyclopentadienyl(−1) ligand [35]. This complex displays magnetic hysteresis above liquid-nitrogen temperatures, possessing an effective energy barrier for magnetization reversal, $\Delta_{\text{eff}}/k_{\text{B}}$, of 2217 K and blocking temperatures, T_{B} (at 100 s, 65 K) that reach temperatures practical for the development of nanomagnet devices. The great success of Ln(III)s to design SMMs is due to their contracted valence 4f orbitals, a feature that affects both structural and magnetic characteristics [36–38]. These orbitals engage in weak, mainly electrostatic interactions with ligands' orbitals and are thus nearly degenerate in energy, leading to impressive single-ion magnetic anisotropies in Ln(III) complexes. This characteristic is in contrast to d-metal complexes, where covalent interactions between diffuse metal orbitals and ligands quench the orbital angular momentum. Control of the Ln^{III} coordination geometry is thus essential to the construction of SMMs. For example, strongly axial ligand fields can maximize Δ_{eff} for oblate [24] Tb^{III} and Dy^{III} centers and reduce transverse anisotropy, which can in turn decrease the rate of magnetization relaxation through the energy barrier by quantum tunneling. Attaining a high symmetry is also valuable for complexes containing non-Kramers Ln^{III} centers (metal ions with integer spin), e.g., Tb^{III} ($4f^8$, $S = 3$) for which $\pm M_J$ degeneracy is not guaranteed [38].

Dinuclear Ln(III) complexes are the simplest molecular entities which allow the in-depth investigation of magnetic Ln^{III}...Ln^{III} exchange interactions [39], which are generally very weak. Scientists have been trying to elucidate the nature and strength of these interactions, as well as the alignment of spin vectors and anisotropy axes; such parameters are affected by the coordination geometries of the Ln^{III} centers, the molecular symmetry and/or the nature of the bridging ligands. Moreover, Ln^{III}₂ SMMs are ideal model systems for providing answers to fundamental questions regarding the paramagnetic slow relaxation from the whole molecule or half of the molecule involving two or a single Ln^{III} center, respectively. Another exciting area to which Ln^{III}₂ complexes are highly relevant is quantum computation [40–42]. One of the main strategies is the design of dinuclear complexes of anisotropic metal ions (hence some Ln^{III} ions are ideal candidates), exhibiting dissimilar coordination environments and very weak magnetic coupling. However, the preparation of asymmetric Ln^{III}₂ complexes is by no means easy, because nature often favors symmetric molecules. Asymmetric dinuclear Ln(III) complexes are also valuable, because they allow detailed studies on the two possible thermally activated relaxation processes of molecular origin that are often observed in Ln(III) SMMs [43–45].

For the above-mentioned reasons, it is evident that the synthesis of asymmetric Ln^{III}₂ complexes is desirable [42–46]. The design principle behind the implementation of this goal is the appropriate choice of the bridging organic ligand, which should be ditopic. Such a ligand introduces preprogrammed

coordination information that is “stored” within its two coordination pockets. When the ligand reacts with a Ln^{III} ion, the reaction interprets this information according to the metal ion’s own coordination “algorithm”. If: (i) the ligand contains one monoanionic bridging atom or group between asymmetrically disposed terminal coordination sites; (ii) it is not very bulky, thus favoring the incorporation of two ligands per dinuclear moiety; (iii) the same pocket of each ligand is coordinated to a single Ln^{III} center (this of course requires a “favorable” serendipity); and (iv) anionic chelating co-ligands are present to saturate the coordination and charge requirements of the Ln^{III} ion, then asymmetric dinuclear complexes will be expected.

The ligand of choice in the present study, which seems to fulfil the first three of the above mentioned criteria, is *N'*-(1-(pyridin-2-yl)ethylidene)pyridine-2-carbohydrazide, shown in its enol-imino form in Figure 1 and abbreviated as HL, and other names of this compound are 2-acetylpyridine picolinoylhydrazone or methyl(pyridin-2-yl)methanone picolinoylhydrazone. This ditopic ligand can be considered as an asymmetric diazine [47] possessing both bidentate and tridentate coordination pockets. The deprotonated ligand (L^-) has two potentially bridging functionalities ($\mu\text{-O}$, $\mu\text{-N-N}$) and, due to the free rotation around the single *N-N* bond, can exist in two different coordination conformers, both of which can in principle give dinuclear complexes (but also polynuclear ones). It was hoped that the deprotonated alkoxido oxygen atom (a “hard” base according to the HSAB principle) would be the bridging one towards the Ln^{III} ions (“hard” acids) leaving the closest nitrogen atom of the central backbone free, i.e., non-coordinated; this, indeed, turned out to be the case (vide infra). In addition to the designed criteria discussed above, we decided to work with this ligand for three additional reasons: (a) its published coordination chemistry (a recent report is from our group [48]) remains limited [47–55]; (b) three mononuclear Ln(III) complexes, namely $[\text{Ln}(\text{NO}_3)_3(\text{HL})(\text{MeOH})_2]$ ($\text{Ln} = \text{La}, \text{Ce}$) and $[\text{Nd}(\text{NO}_3)_3(\text{HL})(\text{H}_2\text{O})]\cdot\text{MeOH}$, possessing the tridentate chelating $\text{N}_{\text{pyridyl}}, \text{N}, \text{O}$ (1.10011 using Harris notation [56], Figure 2), neutral ligand in its keto-amino form, had already been structurally characterized [50] (it was our belief that Ln(III) complexes containing the anionic L^- ligand could exist); and (c) somewhat similar ligands derived from the condensation of picolinic acid hydrazide and other carbonyl-containing compounds have given Ln^{III}_2 complexes with remarkable magnetic properties [43,44].

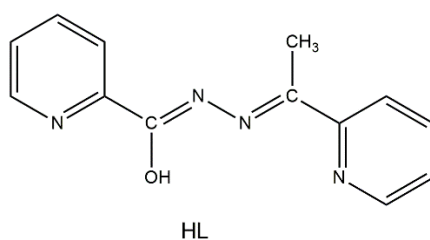


Figure 1. Structural formula of the free ligand *N'*-(1-(pyridin-2-yl)ethylidene)pyridine-2-carbohydrazide, drawn in its enol-imino tautomer, and its abbreviation.

Taking into account the above information, we report in this paper on the reactions between hydrated gadolinium(III), terbium(III), dysprosium(III) and erbium(III) nitrates and LH, which have led to the desired asymmetric dinuclear complexes. The complexes were characterized by single-crystal X-ray diffraction and conventional spectroscopic methods, while special attention was given to the study of their magnetic properties. This work can be considered as a continuation of the interest of our group in the chemistry, magnetism, and catalytic and photophysical properties of Ln^{III}_2 complexes [57–67], some of which are asymmetric [62,64–66].

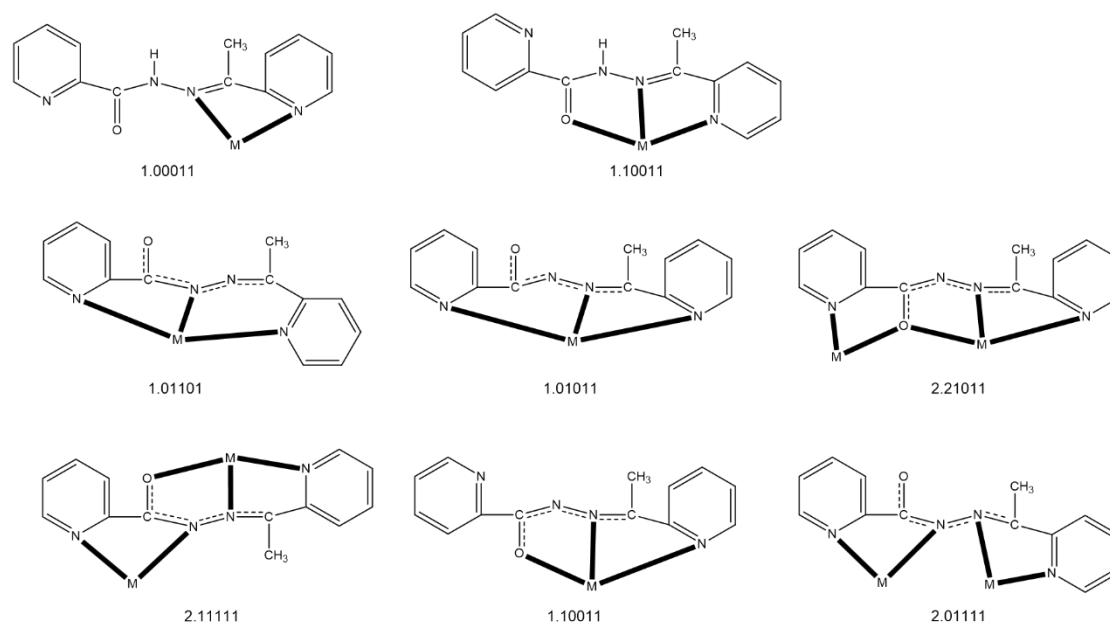


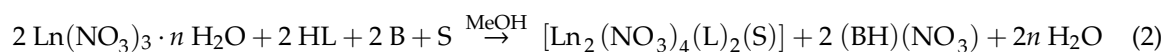
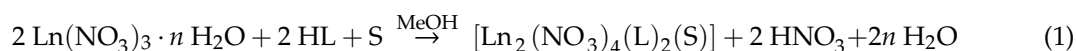
Figure 2. To date the crystallographically confirmed ligation modes of HL or L^- , and the Harris notation that describes these modes. The neutral ligand exists in the keto-amino form in the complexes. In the anionic ligand, the central OCNNC backbone has been drawn in a manner that emphasizes its delocalized nature which appears in most complexes. The coordination bonds are drawn with bold lines. M = metal ion. The structurally characterized complexes are listed in Table 3.

2. Results and Discussion

2.1. Synthetic Comments and Conventional Spectroscopic Characterization

We decided to use lanthanide(III) nitrates as starting materials, because the nitrate groups are excellent chelating capping ligands in Ln(III) chemistry. A variety of $\text{Ln}(\text{NO}_3)_3 \cdot n\text{H}_2\text{O}/\text{LH}$ ($\text{Ln} = \text{Gd}-\text{Yb}$) reactions systems, involving various solvent media, reagent ratios, absence/presence of external base and crystallization methods were systematically studied before establishing the optimized experiments described in Section 3. The only solvent that gave satisfactory crystallinity was methanol. In many instances, we isolated microcrystalline powders with acceptable analytical data, but we report here only the structurally characterized products which are Gd(III), Tb(III), Dy(III), and Er(III) complexes.

The 1:1 reactions between $\text{Ln}(\text{NO}_3)_3 \cdot n\text{H}_2\text{O}$ ($n = 5, 6$) and HL in MeOH gave pale yellow solutions from which yellowish crystals of $[\text{Gd}_2(\text{NO}_3)_4(\text{L})_2(\text{H}_2\text{O})] \cdot 2\text{MeOH} \cdot 2\text{H}_2\text{O}$ (1·2MeOH·2H₂O), $[\text{Tb}_2(\text{NO}_3)_4(\text{L})_2(\text{H}_2\text{O})] \cdot 2\text{MeOH} \cdot 1.5\text{H}_2\text{O}$ (2·2MeOH·1.5H₂O), $[\text{Dy}_2(\text{NO}_3)_4(\text{L})_2(\text{MeOH})_{0.7}(\text{H}_2\text{O})_{0.3}] \cdot 2.5\text{MeOH}$ (3·2.5MeOH) and $[\text{Er}_2(\text{NO}_3)_4(\text{L})_2(\text{H}_2\text{O})] \cdot 3\text{MeOH} \cdot 0.5\text{H}_2\text{O}$ (4·3MeOH·0.5H₂O) were subsequently isolated in moderate to good yields. Unit-cell determination of poor-quality crystals of the Eu(III) complex proved that this is most probably isomorphous to 1·2MeOH·2H₂O. Assuming that the complexes are the only products from the reaction system, their formation can be summarized by Equation (1); S is H₂O for the Gd(III), Tb(III) and Er(III) complexes, and MeOH/H₂O for the Dy(III) compound (vide infra). Use of bases, e.g., Et₃N ($\text{Ln}^{\text{III}}:\text{ligand}:\text{base} = 1:1:1$), gave the same complexes (by analytical data and IR evidences) in a powder form, Equation (2). The dried samples were used for the IR and UV/Vis spectra, whereas the as-isolated crystals were used for the magnetic measurements.



When the reactions are performed as illustrated in Equation (1) with La(III), Ce(III), Pr(III) and Nd(III), single crystals of $[\text{Ln}(\text{NO}_3)_3(\text{HL})(\text{MeOH})_2]$ ($\text{Ln} = \text{La}, \text{Ce}$) [50], $[\text{Nd}(\text{NO}_3)_3(\text{HL})(\text{H}_2\text{O})]\cdot\text{MeOH}$ [50] and $[\text{Pr}(\text{NO}_3)_3(\text{HL})(\text{H}_2\text{O})]\cdot\text{MeOH}$ were obtained. The identity of the La(III), Ce(III) and Nd(III) complexes was confirmed by the unit cell comparisons with those of the reported materials [50], while the unit cell dimensions of the Pr(III) compound (which was not reported by Xu et al.) are very similar to those of its Nd(III) counterpart. We attribute the difference in the identity of the La(III)-Nd(III) and Eu(III)-Dy(III), Er(III) complexes to the smaller polarizing ability of the lighter and larger Ln^{III} ions, whose weaker coordination to the oxygen atom of the enol-imino form of LH in solution is not enough to remove the acidic hydrogen atom from the -OH group. In contrast to what was reported in the literature [50], when Et_3N is used in the reaction mixtures involving La(III), Ce(III), Pr(III) and Nd(III) ions with HL in MeOH (i.e., reactions analogous to those described by Equation (2)), powders of uncertain nature are isolated. Their characterization could not be proceeded further; their IR spectra, however, resemble those of 1–4 suggesting deprotonation of the ligand.

In the IR spectra of the well-dried samples 1–4, the broad band centered at $\sim 3420\text{ cm}^{-1}$ is due to the $\nu(\text{OH})$ vibration of coordinated H_2O (1–4) or MeOH (3) [48], while the $\delta(\text{OH})$ vibrations appear at $\sim 1615\text{ cm}^{-1}$. The medium-intensity band at 3316 cm^{-1} and the very strong band at 1702 cm^{-1} in the spectrum of the free ligand HL are assigned to the $\nu(\text{NH})$ and $\nu(\text{C}=\text{O})$ vibrations, respectively [47,54]. These bands suggest that HL, whose crystal structure is not known, exists in its keto-amino form in the solid state, and not in the enol-imino form shown in Figure 1. There are no bands in the regions $3400\text{--}3100$ and $1720\text{--}1625\text{ cm}^{-1}$ regions of the spectra for 1–4, indicating that the carbon-oxygen bond of coordinated L^- does not have an appreciable double bond character [67]. This conclusion is also supported by the single-crystal X-ray structures of the complexes (vide infra). The highest wavenumber bands in the $1600\text{--}400\text{ cm}^{-1}$ region are at 1594 (1–3) and 1596 cm^{-1} (4), assigned to a pyridyl stretching vibration [48]. The bands at ~ 1470 and $\sim 1280\text{ cm}^{-1}$ are assigned [68,69] to the $\nu_1(\text{A}_1)[\nu(\text{N}=\text{O})]$ and $\nu_5(\text{B}_2)[\nu_{\text{as}}(\text{NO}_2)]$ modes, respectively, of the coordinated nitrate group. The separation of these two, highest-frequency stretching bands is large ($\sim 190\text{ cm}^{-1}$), indicating the bidentate character of the nitrate ligands [68]. The IR spectra of the crystalline samples (i.e., those containing lattice solvent molecules) are very similar with those of the fully dried samples in the $3500\text{--}2800\text{ cm}^{-1}$ region and almost identical in the $1700\text{--}400\text{ cm}^{-1}$ region.

The solid-state (diffuse reflectance) spectra of 2–4 (Figure 3) are dominated by broad intraligand bands in the $280\text{--}430\text{ nm}$ range. The f-f transitions could be seen, and these have been assigned on the basis of the well characterized energy-level diagrams [70–72] for the Ln^{III} ions concerned [70–72]. Specific assignments are as follows (the wavelengths are in parentheses): Complex 2: ${}^7\text{F}_6 \rightarrow {}^7\text{F}_3$ (1987 nm); ${}^7\text{F}_6 \rightarrow {}^7\text{F}_2$ (1915 nm); ${}^7\text{F}_6 \rightarrow {}^7\text{F}_1$ (1848 nm); ${}^7\text{F}_6 \rightarrow {}^7\text{F}_0$ (1654 nm), ${}^7\text{F}_6 \rightarrow {}^5\text{D}_4$ (490 nm, sh). Complex 3: ${}^6\text{H}_{15/2} \rightarrow {}^6\text{H}_{11/2}$ (1702 nm); ${}^6\text{H}_{15/2} \rightarrow {}^6\text{H}_{9/2}$, ${}^6\text{F}_{11/2}$ (1301 nm); ${}^6\text{H}_{15/2} \rightarrow {}^6\text{F}_{9/2}$, ${}^6\text{H}_{7/2}$ (1100 nm); ${}^6\text{H}_{15/2} \rightarrow {}^6\text{H}_{5/2}$ (975 nm); ${}^6\text{H}_{15/2} \rightarrow {}^6\text{F}_{7/2}$ (910 nm); ${}^6\text{H}_{15/2} \rightarrow {}^6\text{F}_{5/2}$ (811 nm); ${}^6\text{H}_{15/2} \rightarrow {}^6\text{F}_{3/2}$ (757 nm); ${}^6\text{H}_{15/2} \rightarrow {}^6\text{F}_{1/2}$ (738 nm, sh); ${}^6\text{H}_{15/2} \rightarrow {}^4\text{F}_{9/2}$ (480 nm, sh). Complex 4: ${}^4\text{I}_{11/2} \rightarrow {}^4\text{F}_{9/2}$ (1917 nm); ${}^4\text{I}_{15/2} \rightarrow {}^4\text{I}_{13/2}$ (1488 nm); ${}^4\text{I}_{15/2} \rightarrow {}^4\text{I}_{11/2}$ (960 nm); ${}^4\text{I}_{15/2} \rightarrow {}^4\text{I}_{9/2}$ (802 nm); ${}^4\text{I}_{15/2} \rightarrow {}^4\text{F}_{9/2}$ (648 nm); ${}^4\text{I}_{15/2} \rightarrow {}^4\text{S}_{3/2}$ (538 nm); ${}^4\text{I}_{15/2} \rightarrow {}^2\text{H}_{11/2}$ (518 nm); ${}^4\text{I}_{15/2} \rightarrow {}^4\text{F}_{7/2}$ (483 nm). The unusually high intensity of the band assigned to the ${}^4\text{I}_{15/2} \rightarrow {}^2\text{H}_{11/2}$ transition in the spectrum of 4 is due to the fact that this transition is “hypersensitive” [72,73]; the absence of splitting of this band might indicate that the coordination number of Er(III) is higher than 8 in this compound [65,72,73]. The diffuse reflectance spectra of the crystalline samples (i.e., those containing lattice solvent molecules) are identical with those of the fully dried samples.

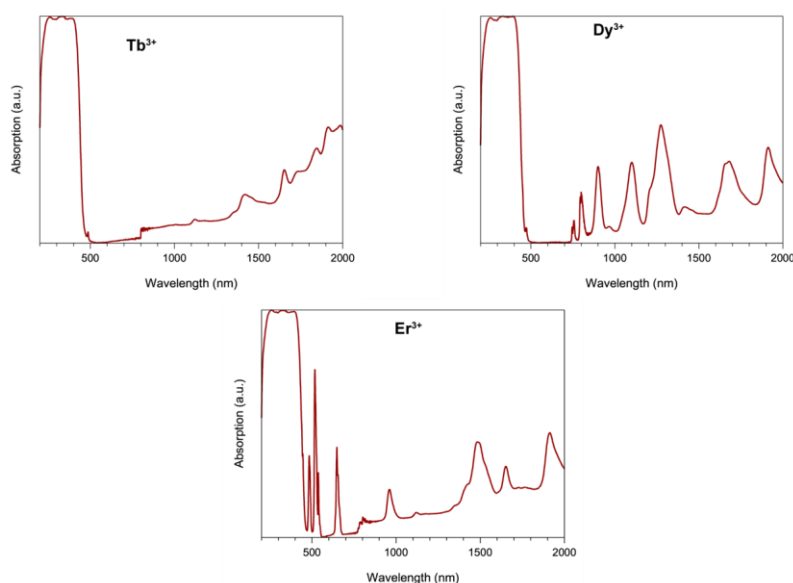


Figure 3. Solid-state (diffuse reflectance) electronic spectra of complexes **2** (top left), **3** (top right) and **4** (bottom) in the 250–2000 nm range.

2.2. Description of Structures

The structures of $1 \cdot 2\text{MeOH} \cdot 2\text{H}_2\text{O}$, $2 \cdot 2\text{MeOH} \cdot 1.5\text{H}_2\text{O}$, $3 \cdot 2.5\text{MeOH}$, and $4 \cdot 3\text{MeOH} \cdot 0.5\text{H}_2\text{O}$ were determined by single-crystal X-ray crystallography. Crystallographic data are listed in Table 1. Various structural plots are shown in Figures 4–6 and Supplementary Figures S1–S5. Selected interatomic distances and bond angles are given in Table 2.

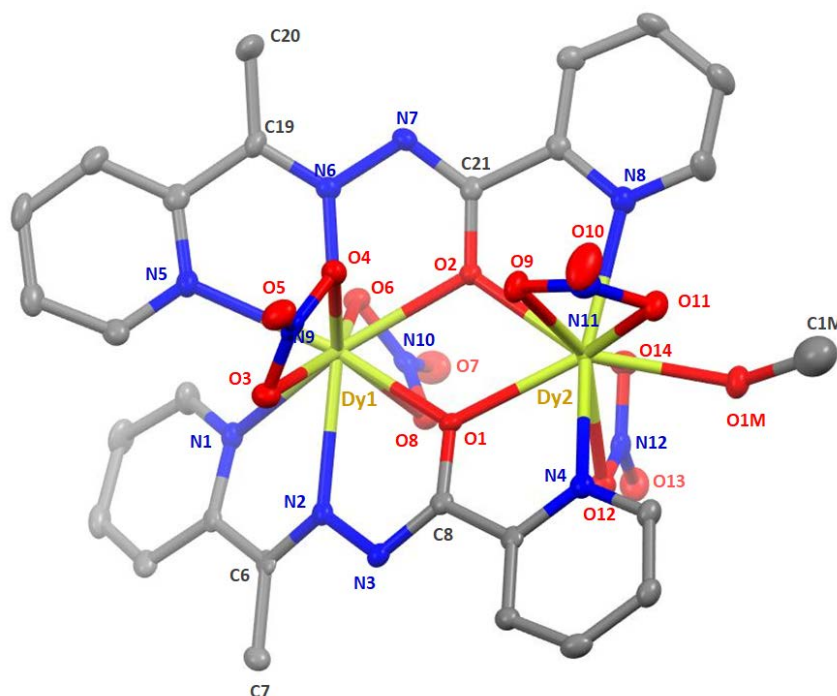


Figure 4. Molecular structure of $[\text{Dy}_2(\text{NO}_3)_4(\text{L})_2(\text{MeOH})]$ as found in $3 \cdot 2.5\text{MeOH}$ at 120 K. Thermal ellipsoids are depicted at 50% probability level. Hydrogen atoms are omitted for clarity. Note that only the major complex is depicted here, i.e., with coordinated MeOH instead of H_2O , C1M having an occupancy of ca. 0.7.

Table 1. Crystallographic data and structural refinement parameters for complexes 1·2MeOH·2H₂O, 2·2MeOH·1.5H₂O, 3·2.5MeOH and 4·3MeOH·0.5H₂O.

Parameter	1·2MeOH·2H ₂ O	2·2MeOH·1.5H ₂ O	3·2.5MeOH	4·3MeOH·0.5H ₂ O
Formula	C ₂₆ H ₂₄ Gd ₂ N ₁₂ O ₁₅ ·2(CH ₄ O)·2(H ₂ O)	(C ₂₆ H ₂₄ Tb ₂ N ₁₂ O ₁₅) ₂ ·4(CH ₄ O)·3(H ₂ O)	(C ₂₇ H ₂₆ Dy ₂ N ₁₂ O ₁₅) ₂ ·5(CH ₄ O)	(C ₂₆ H ₂₄ Er ₂ N ₁₂ O ₁₅) ₂ ·6(CH ₄ O)·(H ₂ O)
Formula weight	1159.19	2307.04	1151.67	2368.45
Crystal color	yellow	yellow	yellow	yellow
Crystal size, mm	0.12 × 0.11 × 0.04	0.20 × 0.17 × 0.06	0.22 × 0.15 × 0.05	0.20 × 0.17 × 0.06
Crystal system	triclinic	triclinic	triclinic	triclinic
Space group	P $\bar{1}$	P $\bar{1}$	P $\bar{1}$	P $\bar{1}$
Temperature, K	120	120	120	120
Radiation, Å	Mo K α , 0.71073	Mo K α , 0.71073	Mo K α , 0.71073	Mo K α , 0.71073
a, Å	10.4504(10)	10.3899(16)	10.3194(8)	10.3551(8)
b, Å	12.3976(12)	12.4185(18)	12.1909(9)	12.4468(10)
c, Å	17.4313(17)	17.609(3)	17.8985(14)	17.7769(13)
α , °	74.879(5)	73.749(7)	71.376(4)	71.992(4)
β , °	85.147(5)	84.738(7)	84.075(4)	83.975(4)
γ , °	68.821(4)	69.114(7)	71.252(4)	69.411(4)
Volume, Å ³	2032.8(3)	2037.8(5)	2020.6(3)	2039.8(3)
Z	2	1	1	1
Calculated density, g·cm ⁻³	1.894	1.880	1.913	1.928
Absorption coefficient, mm ⁻¹	3.325	3.531	3.758	4.176
θ_{\min} – θ_{\max} , °	1.918–29.713	2.098–28.438	2.084–25.505	2.101–30.489
Reflections collected/unique	47128/10876	30434/9998	120082/7400	44288/12236
Completeness to 2 θ	0.940	0.974	0.984	0.996
R_{int}	0.0374	0.0692	0.0600	0.0296
Refined parameters/restraints	563/3	578/2	530/1	587/2
R_1 [$I > 2\sigma(I)$] ^a , wR_2 ^b (all data)	0.0330, 0.0646	0.0545, 0.1100	0.0338, 0.0810	0.0241, 0.0554
Goodness-of-fit on F^2	1.059	1.069	1.107	1.036

$$^a R_1 = \Sigma(|F_o| - |F_c|)/\Sigma|F_o|. \quad ^b wR_2 = \{\Sigma[w(F_o^2 - F_c^2)^2]/\Sigma[w(F_o^2)^2]\}^{1/2}.$$

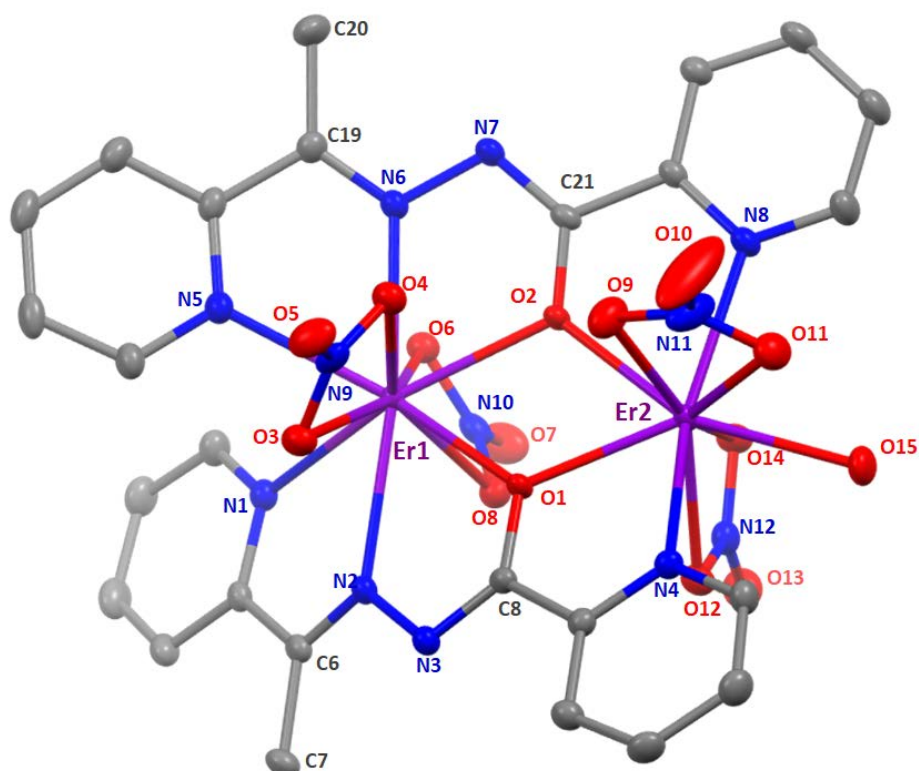


Figure 5. Molecular structure of $[\text{Er}_2(\text{NO}_3)_4(\text{L})_2(\text{H}_2\text{O})]$ as found in $4 \cdot 3\text{MeOH} \cdot 0.5\text{H}_2\text{O}$. Thermal ellipsoids are depicted at 50% probability level. Hydrogen atoms are omitted for clarity.

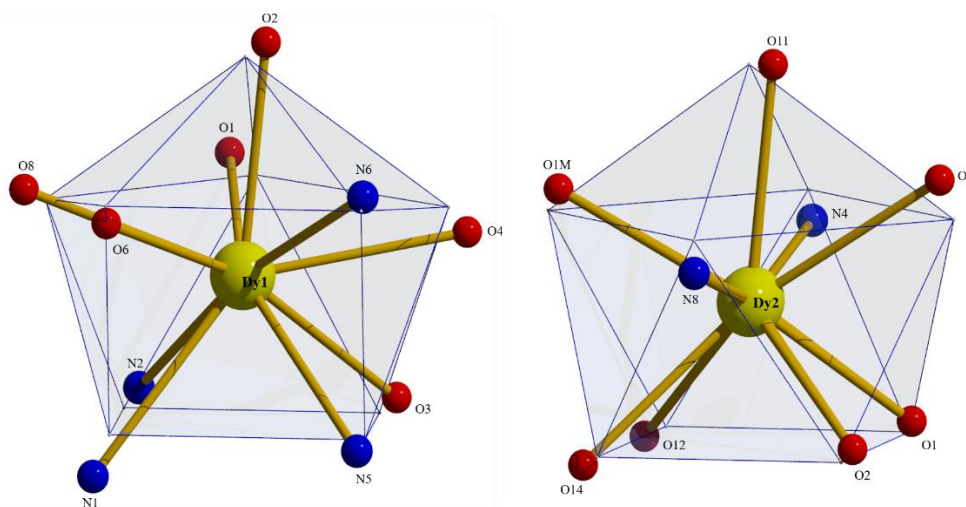


Figure 6. Sphenocoronal and spherical capped square antiprismatic coordination geometries of Dy1 and Dy2, respectively, in the structure of $3 \cdot 2.5\text{MeOH}$. The plotted polyhedra are the ideal, best-fit polyhedra using the program SHAPE [74].

Table 2. Selected interatomic distances (Å) and the Ln-O-Ln bond angles (°) in complexes 1·2MeOH·2H₂O, 2·2MeOH·1.5H₂O, 3·2.5MeOH and 4·3MeOH·0.5H₂O.

Interatomic Distances (Å)				
	Ln = Gd (1·2MeOH·2H ₂ O)	Ln = Tb (2·2MeOH·1.5H ₂ O)	Ln = Dy (3·2.5MeOH)	Ln = Er (4·3MeOH·0.5H ₂ O)
Ln1...Ln2	4.000(1)	3.969(1)	3.945(1)	3.933(1)
Ln1-O3	2.583(3)	2.574(5)	2.586(4)	2.557(2)
Ln1-O4	2.500(3)	2.475(5)	2.468(4)	2.448(2)
Ln1-O6	2.492(2)	2.489(5)	2.468(4)	2.461(2)
Ln1-O8	2.543(3)	2.511(5)	2.485(4)	2.489(2)
Ln1-O1	2.394(2)	2.378(4)	2.359(4)	2.343(2)
Ln1-O2	2.389(2)	2.380(5)	2.364(3)	2.347(2)
Ln1-N1	2.653(3)	2.632(7)	2.614(5)	2.610(2)
Ln1-N2	2.573(3)	2.551(6)	2.523(4)	2.517(2)
Ln1-N5	2.550(3)	2.533(6)	2.534(5)	2.514(2)
Ln1-N6	2.547(3)	2.534(6)	2.512(4)	2.506(2)
Ln2-O9	2.488(3)	2.470(5)	2.462(4)	2.451(2)
Ln2-O11	2.458(3)	2.465(5)	2.436(4)	2.443(2)
Ln2-O12	2.472(3)	2.457(5)	2.443(4)	2.435(2)
Ln2-O14	2.472(3)	2.452(5)	2.439(4)	2.418(2)
Ln2-O1	2.353(2)	2.337(5)	2.326(3)	2.310(2)
Ln2-O2	2.383(2)	2.361(4)	2.348(4)	2.344(2)
Ln2-N4	2.562(3)	2.545(5)	2.509(5)	2.505(2)
Ln2-N8	2.528(3)	2.511(6)	2.503(5)	2.478(2)
Ln2-O15/O1M	2.402(3)	2.383(5)	2.383(4)	2.347(2)
C6-N2	1.289(5)	1.301(9)	1.297(7)	1.295(3)
N2-N3	1.411(4)	1.406(7)	1.403(6)	1.411(3)
N3-C8	1.294(5)	1.277(9)	1.302(7)	1.302(3)
C8-O1	1.308(4)	1.309(8)	1.299(6)	1.307(3)
C19-N6	1.290(4)	1.292(9)	1.314(7)	1.292(3)
N6-N7	1.398(4)	1.386(8)	1.396(6)	1.402(3)
N7-C21	1.303(4)	1.311(8)	1.292(7)	1.305(3)
C21-O2	1.313(4)	1.304(8)	1.309(6)	1.310(3)
Ln-O-Ln Bond Angles (°)				
Ln1-O1-Ln2	114.8(1)	114.7(2)	114.7(1)	115.4(1)
Ln1-O2-Ln2	113.9(1)	113.7(2)	113.7(1)	113.9(1)

As shown by Figures 4 and 5 and Supplementary Figures S1 and S2, the four complexes have similar molecular structures. The main difference is that the Gd(III), Tb(III), and Er(III) complexes contain one coordinated aqua ligand that is replaced by a mixture of coordinated H₂O and MeOH molecules in the Dy(III) complex, with a ca. 30%: 70% ratio ($\pm 15\%$). This ratio has been observed on two different crystals. Despite very close metrics for the unit cells (Table 1), the four complexes differ slightly by their lattice solvent contents. A general description of the molecular structures is given below.

In the dinuclear molecules, the two Ln^{III} ions are doubly bridged by the deprotonated oxygen atoms (O1, O2) of the two parallel (or “head-to-head”) 2.21011 ligands (Figure 2). The Ln^{III}...Ln^{III} distances fall in the 4.000(1)–3.933(1) Å range, while the Ln-O-Ln bond angles are in the narrow 113.7(2)–115.4(1)° range. The central {Ln₂(μ -OR)₂}⁴⁺ core appears to be nearly rhombic. Two pyridyl nitrogen (N1, N5) and two “imino” nitrogen atoms (N2, N6), as well as two slightly anisobidentate chelating nitrato groups (O3/O4, O6/O8) complete 10-coordination at Ln1 creating a {Ln1O₆N₄} coordination environment. The {Ln2O₇N₂} 9-coordinate environment at Ln2 is completed by two pyridyl nitrogen atoms (N4, N8), two almost symmetrical bidentate chelating nitrato groups (O9/O11, O12/O14) and one terminal aquo (for 1·2MeOH·2H₂O, 2·2MeOH·1.5H₂O and 4·3MeOH·0.5H₂O) or methanol (3·2.5MeOH) ligands (the donor atom is O15 or O1M). For a given bond, the Ln-O/N bond

lengths generally follow the Gd > Tb > Dy > Er order due to lanthanide contraction; this trend is also observed for the Ln...Ln distances. Establishing the site of deprotonation is often difficult for L⁻ and related polydentate ligands [48], but the C8-O1 (average 1.305 Å), N3-C8 (average 1.294 Å), N2-N3 (average 1.408 Å), C6-N2 (average 1.296 Å) and C21-O2 (average 1.309 Å), N7-C21 (average 1.304 Å), N6-N7 (average 1.396 Å), C19-N6 (average 1.297 Å) distances indicate a charge delocalization within the OCNNC backbone of the two deprotonated ligands. If the deprotonation must be localized on a specific atom, the relatively long C8-O1 (average 1.305 Å) and C21-O2 (average 1.309 Å) distances, which are not typical of a coordinated carbonyl group, let us believe that the O atoms are the principal sites of deprotonation.

To evaluate in more detail the coordination polyhedra defined by the donor atoms around Ln1 and Ln2, the experimental structural data were compared to the theoretical values for the most common polyhedra with ten and nine vertices using SHAPE [74]. The so-named continuous shape measures (CShM) approach allows researchers to numerically estimate how far an experimental coordination sphere of a metal ion deviates from an ideal polyhedron. Of the accessible 10-coordinate polyhedra for metal centers, the sphenocorona (tetradecahedron) is the most appropriate for the description of the 10 donor atoms around Ln1 in the four compounds. The best fit for the Ln2 ions was obtained for the spherical capped square antiprism, with the nitrate oxygen atom O11 being the capping atom. Since the nitrate groups impose a small bite angle, the polyhedra of the Ln^{III} centers in the four compounds are distorted [69]. The polyhedra of Dy1 and Dy2 in 3·2.5MeOH are shown in Figure 6, while numerical data are listed in Supplementary Tables S1 and S2.

In the crystal structures, the lattice and coordinated H₂O and MeOH molecules are *H*-bonded connecting the complexes into 3D *H*-bonded networks for 1·2MeOH·2H₂O and 2·2MeOH·1.5H₂O, and an 1D *H*-bonded network for 4·3MeOH·0.5H₂O. Because the solvents are highly disordered with partial occupancies for 3·2.5MeOH (vide infra), its exact dimensionality remains undetermined (1D or higher).

Complexes 1–4 join the family of crystallographically characterized metal complexes based on HL or L⁻ as ligands. The members of this family are listed in Table 3 along with information about the coordination mode of the ligands, the nuclearity and dimensionality of the compounds, and the coordination polyhedra of the metal centers involved. The 2.21011 ligation mode observed for the present dinuclear Ln(III) complexes has been identified in Mn(II), Ni(II) and Cu(II) (2 × 2) grids [47,48,54,55] and in the pentanuclear Mn(II) complex [Mn₅(L)₆](ClO₄)₄ [54], in which the metal ions define a trigonal bipyramid. Totally, six different coordination modes of the anionic L⁻ ligand have been confirmed (Figure 2, Table 3), suggesting that this polydentate ligand is quite flexible; these results imply that, in addition to the criteria discussed in Section 1, serendipity (i.e., the “head-to-head” disposition of the two L⁻ ligands) played also a role in the formation of asymmetric Ln^{III}₂ species.

Table 3. To date crystallographically characterized metal complexes of HL and L⁻, and relevant structural information.

Compound ^a	Coordination Mode ^{b,c}	Nuclearity /Dimensionality	Coordination Geometry ^d	Ref.
[CdBr ₂ (HL)]	1.10011	Mononuclear	tbp	[49]
[Ln(NO ₃) ₃ (HL)(MeOH) ₂] (Ln = La, Ce)	1.10011	Mononuclear	cpa	[50]
[Nd(NO ₃) ₃ (HL)(H ₂ O)]	1.10011	Mononuclear	bsa	[50]
[PdCl ₂ (HL)]	1.01100	Mononuclear	sp	[51]
[HgX ₂ (HL)] (X = Cl, Br)	1.10011	Mononuclear	spy	[52]
[HgI ₂ (HL)(H ₂ O)]	1.10011	Mononuclear	oct	[52]
{[Pb ₃ Br ₆ (HL) ₂]} _n	1.10011	1D (metal-organic ribbon)	7-coordinate ^e , oct	[53]
[PdCl(L)]	1.01011	Mononuclear	sp	[51]
[PdCl(L)]	1.01100	Mononuclear	sp	[51]
[Cu ₄ (L) ₄ (H ₂ O) ₂](NO ₃) ₄	2.21011, 2.11111	Rectangular [2 × 2] grid	spy, oct	[47]
[Mn ₄ (CF ₃ SO ₃)(L) ₄ (H ₂ O) ₃](CF ₃ SO ₃) ₃	2.21011	Square [2 × 2] grid	oct	[54]
[Mn ₅ (L) ₆](ClO ₄) ₄	2.21011	Trigonal bipyramidal topology	oct	[54]
[Mn ₄ (N ₃) ₄ (L) ₄]	2.21011	Square [2 × 2] grid	oct	[55]
[Cu ₄ Br ₂ (L) ₄]Br ₂	2.21011, 2.11111	Rectangular [2 × 2] grid	spy, oct	[48]
[Ni ₄ (NO ₃) ₂ (L) ₄ (H ₂ O)](NO ₃) ₂	2.21011	Square [2 × 2] grid	oct	[48]
[Co ₂ (L) ₃](ClO ₄) ₃	2.01111	Dinuclear helicate	oct	[48]
[Co(L) ₂](ClO ₄)	1.10011	Mononuclear	oct	[48]
[Ln ₂ (NO ₃) ₄ (L) ₂ (H ₂ O)] (Ln = Gd, Tb, Er)	2.21011	Dinuclear	sph, scsa	this work
[Dy ₂ (NO ₃) ₄ (L) ₂ (MeOH)]	2.21011	Dinuclear	sph, scsa	this work

^a Lattice solvent molecules have been omitted. ^b Using the Harris notation. ^c The coordination modes are shown in Figure 2. ^d Abbreviations: sp = square planar; spy = square pyramidal; tbp = trigonal bipyramidal; oct = octahedral; cpa = capped pentagonal antiprismatic; bsa = bicapped square antiprismatic; sph = sphenocorona; scsa = spherical capped square antiprismatic.

2.3. Dc Magnetic Susceptibility Studies

Direct-current (dc) magnetic susceptibility (χ) data on polycrystalline samples of 1·2MeOH·2H₂O, 2·2MeOH·1.5H₂O, 3·2.5MeOH and 4·3MeOH·0.5H₂O were collected in the 1.8–300 K range using an applied field of 0.1 T. Magnetization (M) vs. magnetic field (H) at various low temperatures and vs. HT^{-1} (T is the absolute temperature) measurements were also performed. These magnetic data are shown in Figure 7 and Supplementary Figures S6–S9. For all complexes, the observed paramagnetism arises solely from the 4f Ln^{III} ions. At room temperature, the χT values of 1·2MeOH·2H₂O, 2·2MeOH·1.5H₂O, 3·MeOH·2H₂O and 4·3MeOH·0.5H₂O are 15.9, 23.0, 27.7 and 22.5 cm³·K·mol⁻¹, respectively. These values are in very good agreement with the expected theoretical values (15.75, 23.63, 28.34, 22.96 cm³·K·mol⁻¹, respectively) for two noninteracting Ln^{III} centers: Gd^{III} (⁸S_{7/2}, $S = 7/2$, $L = 0$, $g = 2$), Tb^{III} (⁷F₆, $S = 3$, $L = 3$, $g_J = 3/2$), Dy^{III} (⁶H_{15/2}, $S = 5/2$, $L = 5$, $g_J = 4/3$) and Er^{III} (⁴I_{15/2}, $S = 3/2$, $L = 6$, $g = 6/5$).

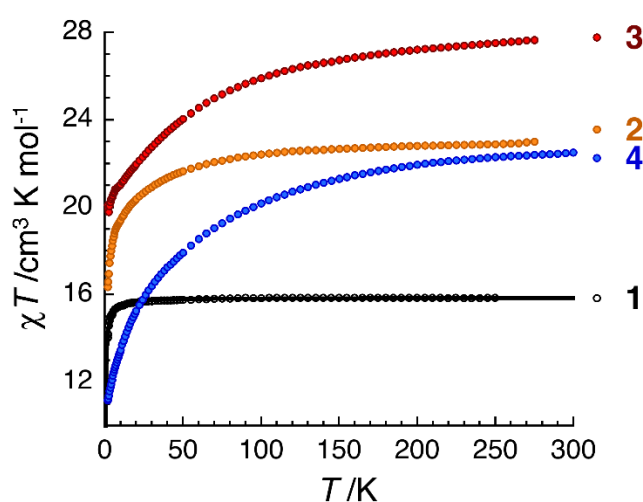


Figure 7. Temperature dependence of the χT product for the four complexes (1·2MeOH·2H₂O, in black; 2·2MeOH·1.5H₂O in orange; 3·2.5MeOH in red and 4·3MeOH·0.5H₂O in blue) discussed in this paper at 0.1 T (χ is defined as M/H per mole of the respective complex). The solid black line is the fit of the data to the theoretical Heisenberg model for a dinuclear Gd^{III}₂ complex; see the text for details.

The presence/absence of magnetic exchange interaction between the two Ln^{III} and its strength in the dinuclear complexes can be revealed looking at the magnetic properties of the Gd(III) complex 1, as the Gd^{III} centers present no spin-orbit coupling at the first order. The decrease of the χT product below ~30 K (the value of the product is 14.0 cm³·K·mol⁻¹ at 1.85 K) reveals directly the presence of antiferromagnetic Gd^{III}...Gd^{III} exchange interactions. The experimental data were fitted to the van Vleck analytical expression of the susceptibility derived from the following isotropic Heisenberg spin Hamiltonian: $H = -2J(S_{Gd1} \cdot S_{Gd2})$. The best-fit parameters obtained are $J/k_B = -0.020(6)$ K and $g = 2.023(1)$. The observed antiferromagnetic exchange interaction is very weak as a consequence of the shielded 4f orbitals that have little overlap with the orbitals of the bridging oxygen atoms. Such very small J values have been observed in systems containing symmetrically-bridged {Gd^{III}₂(μ_2 -OR)₂} cores [57,59,62,75,76]. However, the low symmetry of the Gd^{III} ion in 1 might give rise to small zero-field splitting and this, in turn, can also lead to the decrease of the χT product at low temperatures that would be phenomenologically included the J estimation [75].

Magnetization measurements at 1.85 K (Supplementary Figure S6) reveal a saturation of 14.1 μ_B at 7 T, in very good agreement with the expected theoretical value of 14.0 μ_B for two $S = 7/2$ spins ($g = 2.00$). Indeed, as the interdimer antiferromagnetic interaction is very weak, the magnetization data below 8 K are perfectly fitted to the sum of two $S = 7/2$ Brillouin functions with $g = 2.03(3)$ (Supplementary Figure S6).

For the Tb(III), Dy(III) and Er(III) analogues, the χT product decreases upon cooling of the sample (Figure 7). The values of the χT product at 1.85 K and 0.1 T are 16.4, 20.1 and 11.2 $\text{cm}^3 \cdot \text{K} \cdot \text{mol}^{-1}$ for 2·2MeOH·1.5H₂O, 3·2.5MeOH and 4·3MeOH·0.5H₂O, respectively. For these Ln^{III} ions with an unquenched orbital moment associated with a ligand field, there are three possible contributions to the observed behavior [75]: (a) the thermal depopulations of the Stark sublevels; (b) antiferromagnetic exchange interactions between the magnetic Ln^{III} centers; and (c) the presence of significant magnetic anisotropy. The magnetization values at 1.85 K and 7 T are 10.1, 10.6 and 9.8 μ_B for 2·2MeOH·1.5H₂O, 3·2.5MeOH and 4·3MeOH·0.5H₂O, respectively (Supplementary Figures S7–S9). The non-saturation of the magnetization indicates the presence of significant magnetic anisotropy and/or low-lying excited states in the three complexes [43,44]. This can be further confirmed by the lack of superposition and high-field variation on a single master curve of each M vs. H/T plot (Supplementary Figures S7–S9).

2.4. Ac Magnetic Susceptibility Studies

In order to investigate the presence/absence of slow paramagnetic relaxation, in other words the SMM properties of these complexes, the dynamics of 2·2MeOH·1.5H₂O, 3·2.5MeOH and 4·3MeOH·0.5H₂O was probed by ac susceptometry (Figures 8–10, Supplementary Figures S10–S15). In the zero dc field, an out-of-phase component (χ'') of the ac susceptibility was not detected above 1.8 K for ac frequencies up to 10 KHz. This is also true in presence of external dc fields up to 3 T for 2·2MeOH·1.5H₂O. However, in an applied dc field, clear frequency-dependent in-phase (χ') and out-of-phase signals were detected for 3·2.5MeOH and 4·3MeOH·0.5H₂O (Supplementary Figures S10 and S13). The appearance and the slowing down of the relaxation when applying a small dc field is expected when the magnetization relaxation is dominated by quantum tunneling (quantum tunneling of magnetization, QTM) [3,77] and/or Raman processes [78]. In the QTM case, the application of a dc field minimizes the probability of the magnetization to tunnel, as already observed in many Ln(III) SMMs [18,19,23,34,57,69,79]. The temperature and frequency dependencies of the ac susceptibility were thus studied under an optimum dc field (i.e., a dc field for which the relaxation process of the magnetization exhibits a good compromise between its characteristic time and the intensity of the relaxation mode) of 600 Oe for 3·2.5MeOH and 1000 Oe for 4·3MeOH·0.5H₂O (Figures 8 and 9).

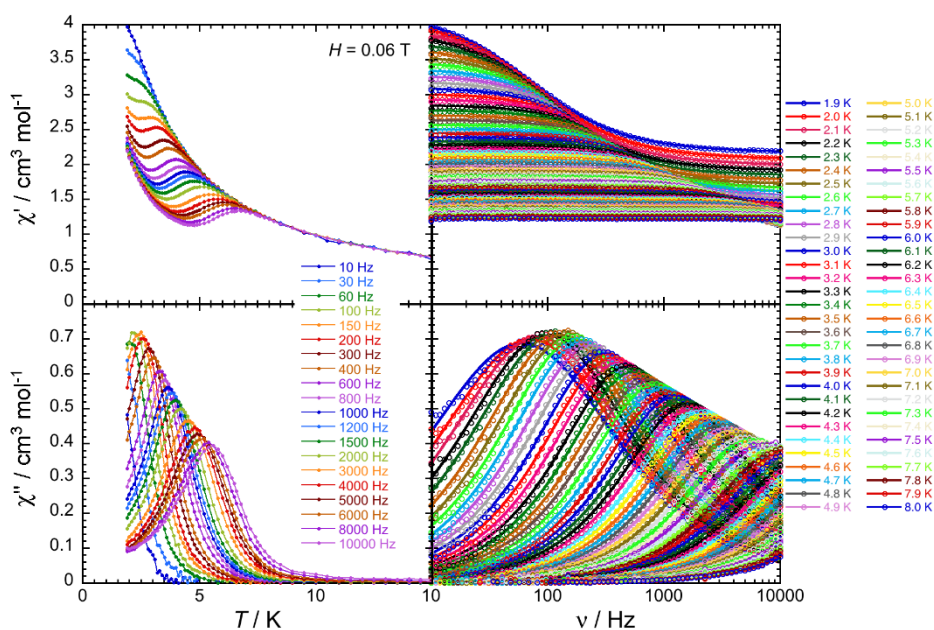


Figure 8. Frequency dependence of the real, in-phase (χ' , **top**) and imaginary, out-of-phase (χ'' , **bottom**) components of the ac susceptibility under an external dc field of 600 Oe (0.06 T) at the indicated temperatures for complex 3·2.5MeOH. Solid lines are visual guides on the left plots, while they show the generalized Debye fit of the ac data on the right.

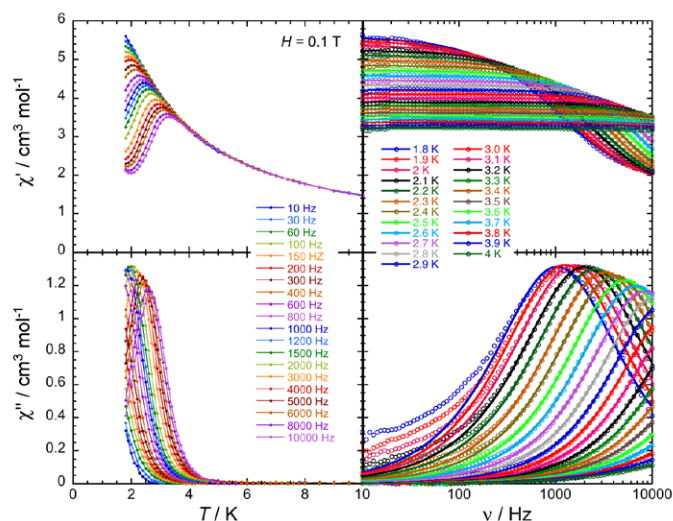


Figure 9. Frequency dependence of the real, in-phase (χ' , **top**) and imaginary, out-of-phase (χ'' , **bottom**) components of the ac susceptibility under an external dc field of 1000 Oe (0.1 T) at the indicated temperatures for complex 4-3MeOH-0.5H₂O. Solid lines are visual guides on the left plots, while they show the generalized Debye fit of the ac data on the right.

The combination of all these frequency dependent ac data (Figures 8 and 9, Supplementary Figures S10 and S13) and their fit to the generalized Debye model [80] allows the determination of the field and temperature dependence of the relaxation time, τ , and its estimated standard deviation (ESD) [81], which quantifies the broadness of the relaxation time distribution. As shown in Figure 10, the obtained ESDs are significantly large and thus the following discussion of the relaxation time must be taken with a certain caution.

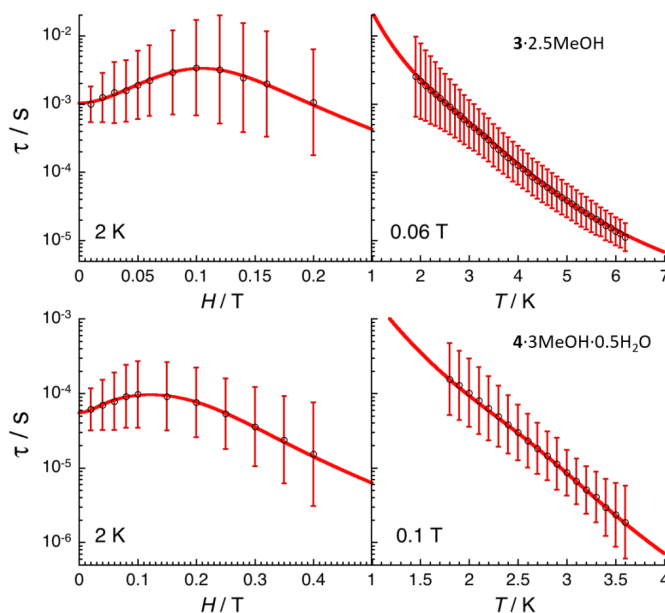


Figure 10. Field (left) and temperature (right) dependencies of the relaxation time (τ) at 2.0 K and in the presence of an applied static field of 0.06 and 1 T for complexes 3-2.5MeOH (top) and 4-3MeOH-0.5H₂O (bottom), respectively. The relaxation time was estimated from the generalized Debye fits of the ac susceptibility data shown in Figures 8 and 9, Figures S10 and S13. The estimated standard deviations of the relaxation time (vertical solid bars) have been calculated from the α parameters of the generalized Debye fit (Figures S11–S15) and the log-normal distribution as described in ref. [81]. The solid red lines are the best fit discussed in the text.

Paramagnetic relaxation [82] usually has four principal origins, which include Raman [78], direct [82], thermally activated (Arrhenius) [82], and QTM [3,77,83,84] relaxation processes, as summarized in the following Equations (3) and (4) [83]:

$$\tau^{-1} = \tau_{Raman}^{-1} + \tau_{Direct}^{-1} + \tau_{Arrhenius}^{-1} + \tau_{QTM}^{-1} \quad (3)$$

$$\tau^{-1} = C \frac{1 + C_1 H^2}{1 + C_2 H^2} T^n + A T H^4 + \tau_0^{-1} \exp\left(-\frac{\Delta}{k_B T}\right) + \frac{B_1}{1 + B_2 H^2} \quad (4)$$

As illustrated by these equations, each relaxation mechanism has its own characteristic temperature (T) and field (H) dependence. The field dependence of the relaxation time, shown on the left part of Figure 10, possesses a similar variation for 3·2.5MeOH and 4·3MeOH·0.5H₂O. At low fields, an increase of the relaxation time is first observed, in agreement with only QTM or Raman (with $C_2 > C_1$) pathways, while the H^4 variation at higher fields strongly suggests a Direct relaxation mechanism. Therefore, to model the experimental field dependence of the relaxation time, two simple approaches have been used considering (i) Raman and direct, and (ii) QTM and direct processes.

Both models are able to reproduce the experimental τ vs. H data, but only the first one, when an Orbach relaxation is introduced, is able to fit both τ vs. H and τ vs. T variations as shown in Figure 10. The best parameters of the three first terms of Equation (4) are for 3·2.5MeOH: $C_1 = 25(5) \text{ T}^{-2}$, $C_2 = 396(50) \text{ T}^{-2}$, $C = 88(5) \text{ s}^{-1} \cdot \text{K}^{-3.4}$, $n = 3.4(1)$, $A = 2.9(4) \times 10^5 \text{ K}^{-1} \cdot \text{T}^{-4} \cdot \text{s}^{-1}$, $\tau_0 = 6.3(5) \times 10^{-8} \text{ s}$ and $\Delta_{\text{eff}}/k_B = 34(2) \text{ K}$; and for 4·3MeOH·0.5H₂O: $C_1 = 222(20) \text{ T}^{-2}$, $C_2 = 461(50) \text{ T}^{-2}$, $C = 652(50) \text{ s}^{-1} \cdot \text{K}^{-4.8}$, $n = 4.8(5)$, $A = 1.2(7) \times 10^6 \text{ K}^{-1} \cdot \text{T}^{-4} \cdot \text{s}^{-1}$, $\tau_0 = 5.6(5) \times 10^{-11} \text{ s}$ and $\Delta_{\text{eff}}/k_B = 39(2) \text{ K}$. Considering the necessity of three relaxation mechanisms with seven adjustable parameters in the above model, alternative descriptions are likely possible, even if we were not able to find another model involving only three relaxation processes. In particular, the origin of an energy gap of 34 K (for 3·2.5MeOH) and 39 K (for 4·3MeOH·0.5H₂O) for these Dy(III) and Er(III) complexes is not obvious and should certainly be questioned in the present model. To conclude this analysis, keeping in mind that it should be taken with great caution as indicated above, these results suggests that Raman, direct and an Orbach-like processes are at the origin of the observed SMM properties in 3·2.5MeOH and 4·3MeOH·0.5H₂O.

At this stage, we are doing a brief parenthesis to mention (for the non-familiar readers) that in a Direct relaxation process [82], a transition between one m_j state to a different one is by emission/absorption of a phonon to/from the surrounding bath, with the same quanta of energy of the transition. This mechanism is efficient at very low temperatures only under an applied magnetic field and it is strongly sample- and Ln^{III}- dependent. The Raman relaxation pathway [78] involves the inelastic scattering of phonons, where the energies of the involved phonons decrease or increase, with the difference in energy ($h\nu_{i+1} - h\nu_i$) being absorbed or released by the system. When the scattered energy causes a direct transition, the respective relaxation process is named first-order Raman, whereas spin relaxation occurring via virtual states is termed second-order Raman mechanism. The Raman pathways require the presence of phonons and become important at finite temperatures. The Raman relaxation mechanisms depend also strongly on the sample and its composition. In the Orbach process [82], the absorption of a phonon by the spin system causes an excitation to a low-lying excited state. This is accompanied by the emission of a phonon with an energy corresponding to the difference between the ground and the low-lying excited state; this provides a pathway for the relaxation between the low-lying states. From the just mentioned processes, only the Orbach one leads to a thermally activated dependence. It is evident that all three magnetization relaxation mechanisms are spin-lattice relaxation processes [82,85].

In an effort to understand the absence of SMM properties at zero field for 3·2.5MeOH, we have determined the orientation of the ground-state magnetic anisotropy axes for the Dy^{III} centers in the complex (Supplementary Figure S16), using a method [25] resulting from an electrostatic model that requires only the knowledge of the single-crystal structure of the complex. Definite conclusions based on the orientations of the anisotropy axes would be risky. Nevertheless for Dy², the easy axis does not

point towards the “axial” O11 atom, which is the capping atom of the capped square antiprismatic polyhedron of this metal ion. This orientation forces the oblate *f*-electron density [24] of Dy²⁺ to be roughly parallel to the easy axis, which is a non-favorable configuration to achieve significant slow magnetization relaxation [25,69]. However, the distribution of the charged oxygen atoms (and the derived field) is rather spherical for both metal ions and any oblate-prolate [24] discussions are perhaps meaningless in the present case.

3. Experimental Section

3.1. Materials, Physical and Spectroscopic Measurements

All manipulations were performed in the normal laboratory atmosphere using reagents and solvents (Alfa Aesar, Aldrich; Karlsruhe, Germany and Tanfrichen, Germany, respectively) as received. The organic ligand LH was synthesized in typical yields of >85% as described in the literature [47,49,51,54], i.e., by the 1:1 reaction between picolinic acid hydrazide and 2-acetylpyridine in refluxing EtOH for 3 h. Its purity was checked by microanalyses (C, H, N), determination of the melting point (found, 192–193 °C; reported 195–197 °C), and IR and ¹H NMR spectra. Elemental analyses (C, H, N) were performed by the University of Patras (Patras, Greece) Center of Instrumental Analysis. FT-IR spectra (4000–400 cm⁻¹) were recorded using a Perkin-Elmer (Perkin-Elmer, Waltham, MA, USA) 16PC spectrometer with samples prepared as KBr pellets. Solid-state electronic (diffuse reflectance) spectra were obtained with an Agilent Cary 5000 instrument (Agilent Technologies, Santa Clara, CA, USA) in the 250–2000 nm range by using an integrating sphere. A KBr reference pellet was prepared by grinding pure KBr (CAS number 7758-02-3, Sigma Aldrich, Athens, Greece, purity >99%) in a pestle and mortar until a homogenous fine powder was obtained. This was then placed in a pellet-forming die under a ~8 tons pressure for about 5 min until a homogenous disc was formed. Discs of the samples of the compounds, mixed and pressed with KBr (roughly 2% in KBr), were prepared in a similar manner. Magnetic measurements were performed on a Quantum Design SQUID magnetometer MPMS-XL (Quantum Design, San Diego, CA, USA) and a PPMS-II susceptometer, housed at the Centre de Recherche Paul Pascal at temperatures between 1.8 and 300 K, and dc magnetic fields ranging from -7 to +7 T. ac magnetic susceptibility measurements were performed in an oscillating ac field of 1 to 6 Oe with frequencies between 10 and 10,000 Hz. The measurements were carried out on polycrystalline samples received directly from the mother liquors (16.70 mg for 1·2MeOH·2H₂O, 13.70 mg for 2·2MeOH·1.5H₂O, 11.76 mg for 3·2.5MeOH and 7.51 mg for 4·3MeOH·0.5H₂O), suspended in mineral oil (typically 10–30 mg) and introduced in a sealed polypropylene bag (3 × 0.5 × 0.02 cm; typically 7–21 mg). Prior to the main experiments, the field-dependent magnetization was measured at 100 K on each sample in order to detect the possible presence of any bulk ferromagnetic impurities. In fact, paramagnetic materials should exhibit a perfect linear dependence of magnetization that extrapolates to zero at zero dc field; all samples appeared to be free of any bulk ferromagnetic impurities. The magnetic data were corrected for the sample holder, the oil and the intrinsic diamagnetic contributions.

3.2. Synthesis of the Representative Complex [Gd₂(NO₃)₄(L)₂(H₂O)]·2MeOH·2H₂O (1·2MeOH·2H₂O)

To a stirred colorless solution of HL (0.024 g, 1.00 mmol) in MeOH (12 mL), solid Gd(NO₃)₃·6H₂O (0.045 g, 1.00 mmol) was added. The solid soon dissolved and the resulting pale yellow solution was stirred for a further 5 min, filtered and stored in a closed flask at room temperature. X-ray quality, yellow crystals of the product were obtained within a period of one week. The crystals were collected by filtration, washed with cold MeOH (2 × 0.5 mL) and Et₂O (4 × 2 mL) and dried in a vacuum desiccator over P₄O₁₀ for 24 h. Yield: 42%. The complex was satisfactorily analyzed as lattice solvent-free, i.e., as **1**. Anal. Calcd. (%) for C₂₆H₂₄N₁₂Gd₂O₁₅: C, 29.48; H, 2.29; N, 15.87. Found (%): C, 29.71; H, 2.24; N, 15.63. IR (KBr, cm⁻¹): 3420mb, 3040w, 3005w, 2920w, 1616m, 1594m, 1576m, 1555sh, 1544m,

1506sh, 1472s, 1445sh, 1358s, 1280sb, 1252sh, 1164m, 1136w, 1100w, 1026m, 1012m, 998w, 920m, 816m, 808sh, 788m, 742m, 708m, 698m, 676m, 636m, 576w, 558w, 518w, 486w, 468m, 418w, 402w.

3.3. Syntheses of the Complexes $[Tb_2(NO_3)_4(L)_2(H_2O)] \cdot 2MeOH \cdot 1.5H_2O$ (2·2MeOH·1.5H₂O), $[Dy_2(NO_3)_4(L)_2(MeOH)] \cdot MeOH \cdot 2H_2O$ (3·2.5MeOH) and $[Er_2(NO_3)_4(L)_2(H_2O)] \cdot 3MeOH \cdot 0.5H_2O$ (4·3MeOH·0.5H₂O)

These complexes were prepared in an identical manner with 1·2MeOH·2H₂O by simply replacing Gd(NO₃)₃·6H₂O with the equivalent amount of the appropriate Ln(NO₃)₃·*n*H₂O (*n* = 5 or 6). The yields were 57, 61 and 48% for the Tb(III), Dy(III) and Er(III) complexes, respectively. The complexes were satisfactorily analyzed as lattice solvent-free, i.e., as **2**, **3**, and **4**. In some samples of the Tb(III) and Dy(III) complexes, a small percentage of lattice H₂O (typically 0.2–0.4 moles per mole of the complex) could also fit the experimental analytical data. The cited experimental values here are for samples found dried from a TGA experiment. Anal. Calcd. (%) for C₂₆H₂₄N₁₂Tb₂O₁₅ (**2**): C, 29.39; H, 2.28; N, 15.82. Found (%): C, 29.21; H, 2.31; N, 15.63. Anal. Calcd. (%) for C₂₇H₂₆N₁₂Dy₂O₁₅ (**3**): C, 29.92; H, 2.42; N, 15.51. Found (%): C, 30.06; H, 2.38; N, 15.40. Anal. Calcd. For C₂₆H₂₄N₁₂Er₂O₁₅ (**4**): C, 28.94; H, 2.25; N, 15.58. Found (%): C, 28.83; H, 2.30; N, 15.32. The IR spectra of these complexes are almost superimposable with the spectrum of **1** with a maximum wavenumber difference of ±4 cm^{−1}.

3.4. Single-Crystal X-ray Crystallography

Crystallographic data (Table 1) were collected with a Bruker APEX II Quasar diffractometer (Bruker Scientific LLC, Billerica, MA, USA), equipped with a graphite monochromator centered on the path of Mo K α radiation. Single crystals of the complexes, obtained as described in Paragraphs 3.2 and 3.3, were coated with Cargille™ NHV immersion oil and mounted on a fiber loop, followed by data collection at 120 or 230 K. The program SAINT was used to integrate the data, which was thereafter corrected using SADABS [86]. The structures were solved using direct methods and refined by a fully-matrix least-squares method on *F*² using SHELXL-2014 [87]. All non-H atoms were refined with anisotropic displacement parameters. Some details are listed below.

For 1·2MeOH·2H₂O: H atoms were assigned to ideal positions and refined isotropically using a riding model, except those of the H₂O and MeOH molecules for which the positions of H atoms were found on the difference Fourier map and refined using positional constraints.

For 2·2MeOH·1.5H₂O: H atoms were assigned to ideal positions and refined isotropically using a riding model, except those of the coordinated H₂O molecule for which the positions of H atoms were introduced based on the different Fourier map. H atoms on some lattice MeOH and H₂O molecules were not introduced but were taken into account in the formula of the complex. Two crystallographically different MeOH molecules were refined with 0.5 occupancies, one of them being very close to a lattice H₂O molecule with a 0.5 occupancy (O19W).

For 4·3MeOH·0.5H₂O: H atoms were assigned to ideal positions and refined isotropically using a riding model, except those of the coordinated H₂O molecule for which the positions of H atoms were introduced based on the difference Fourier map. H atoms on some lattice MeOH and H₂O molecules were not introduced but were taken into account in the formula of the complex. Three crystallographically different MeOH molecules were refined with 0.5 occupancies, one of them being very close to a H₂O molecule with a 0.5 occupancy (O19W).

For 3·2.5MeOH: H atoms were assigned to ideal positions and refined isotropically, except those of the coordinated MeOH molecule for which the positions of H atoms were located on the difference Fourier map and refined using DFIX constraint. The relative electronic densities found on the C and O sites of this coordinated MeOH molecule suggest a cocrystallization of complexes with coordinated methanol and water. The ratio between coordinated MeOH and H₂O was found to be ca. 70%:30% (±15 %) and refined as this. The given formula is taking into account only the major component, i.e., with MeOH only. The crystal structure contains also a large void space that is filled by disordered lattice solvent molecules. As suggested by the interatomic distances, those were refined as lattice

MeOH molecules using DFIX, EADP and SIMU constraints/restraints and with partial occupancies of some of them (1 for C2M/O2M, 0.6 for C3M/O3M disordered on two positions with equal occupancies, 0.5 for C4M/O4M disordered on 2 positions with equal occupancies, and 0.5 for C5M/O5M). H atoms were not introduced when involving disordered solvent molecules, but are taken into account in the compound formula. Due to the use of constraints and partial occupancies, the exact number and nature of those lattice solvent molecules should be taken with care.

Crystallographic data have been deposited with the Cambridge Crystallographic Data Center, No 2002796 (1·2MeOH·2H₂O), 2002794 (2·2MeOH·1.5H₂O), 2002797 (3·2.5MeOH) and 2002795 (4·3MeOH·0.5H₂O). Copies of the data can be obtained free of charge upon application to CCDC, 12 Union Road, Cambridge, CB2 1EZ, UK; Tel.: +(44)-1223-762910; Fax: +(44)-1223-336033; E-mail: deposit@ccdc.cam.ac.uk, or via <http://www.ccdc.cam.ac.uk/conts/retrieving.html>.

4. Concluding Comments and Perspectives

In this work, we have shown that, in addition to the mononuclear complexes [Ln(NO₃)₃(HL)(MeOH)] (Ln = La, Ce) and [Nd(NO₃)₃(HL)(H₂O)] reported earlier [50] where the neutral keto-amino ligand LH behaves as a tridentate chelating, the monoanion L[−] can act as a bridging ligand forming asymmetric dinuclear complexes of the general formula [Ln₂(NO₃)₄(L)₂(S)] (S = H₂O, MeOH). Four analogous complexes (Ln = Gd, Tb, Dy, Er) have been structurally characterized. Complexes 1–4 are new, welcome members of the growing group of complexes containing HL and L[−] (Table 3). This is the main chemical message from our efforts.

The important point of this work from a magnetic point of view is the absence of SMM behavior for the dinuclear Tb(III) complex, while the SMM properties of the Dy(III) and Er(III) analogues can be studied only when a magnetic field is applied. The rather spherical distribution of the charged oxygen atoms (which implies weak magnetic axiality around the oblate Tb^{III} and Dy^{III} centers and weak plane magnetic anisotropy around the prolate Er^{III} ions) is probably responsible for this. For the Dy(III) and Er(III) complexes, the detailed analysis of the relaxation time studying its thermal and field variations reveals the presence of multiple relaxation processes involving a direct relaxation and likely Raman and Orbach-like mechanisms.

We are currently investigating the possibility to prepare polynuclear Ln(III) complexes based on L[−], either “forcing” this ligand to act as triply bridging (μ₃) or/and by using other potentially bridging ancillary ligands. Also, we have been working with bulkier analogues of HL, i.e., by replacing one or both 2-pyridyl groups by 2-quinolyl groups and by using a phenyl group instead of a methyl group, in an effort to reduce the coordination numbers of the Ln^{III} centers in asymmetric dinuclear complexes and achieve slow magnetic relaxation at zero field.

Supplementary Materials: The following are available online, Figure S1: Crystal structure of [Gd₂(NO₃)₂(L)₂(H₂O)] as found in 1·2MeOH·2H₂O at 120 K. Figure S2: The molecule [Tb₂(NO₃)₄(L)₂(H₂O)] that is present in the crystal structure of 2·2MeOH·1.5H₂O. Figure S3: The coordination polyhedra of the two Gd^{III} centers in 1·2MeOH·2H₂O. Figure S4: The coordination polyhedra of the two Tb^{III} centers in 2·2MeOH·1.5H₂O. Figure S5: The coordination polyhedra of the two Er^{III} centers in 4·3MeOH·0.5H₂O. Figure S6: *M* vs. *H* and *M* vs. *H/T* plots for 1·2MeOH·2H₂O. Figure S7: *M* vs. *H* and *M* vs. *H/T* plots for 2·2MeOH·1.5H₂O. Figure S8: *M* vs. *H* and *M* vs. *H/T* plots for 3·2.5MeOH. Figure S9: *M* vs. *H* and *M* vs. *H/T* plots for 4·3MeOH·0.5H₂O. Figure S10: χ' and χ'' vs. ν plots at 2 K for different dc field for 3·2.5MeOH. Figure S11: Field dependence of the parameters, α , χ_0 and χ_∞ , ν and $\chi_0-\chi_\infty$ between 0 and 0.2 T at 2 K for 3·2.5MeOH. Figure S12: Temperature dependence of the parameters, α , χ_0 and χ_∞ , ν and $\chi_0-\chi_\infty$ between 1.8 and 8 K at 0.06 T for 3·2.5MeOH. Figure S13: χ' and χ'' vs. ν plots at 2 K for different dc field for 4·3MeOH·0.5H₂O. Figure S14: Field dependence of the parameters, α , χ_0 and χ_∞ , ν and $\chi_0-\chi_\infty$ between 0 and 0.4 T at 2 K for 4·3MeOH·0.5H₂O. Figure S15: Temperature dependence of the parameters, α , χ_0 and χ_∞ , ν and $\chi_0-\chi_\infty$ between 1.8 and 3 K at 0.1 T 4·3MeOH·0.5H₂O. Figure S16: Ground-state magnetic anisotropy axes for the two Dy^{III} centers in 3·2.5MeOH. Tables S1 and S2: CShM values for the potential polyhedra of Dy1 and Dy2, respectively, in 3·2.5MeOH.

Author Contributions: D.M. and E.P. contributed towards the syntheses, crystallization and conventional characterization of the complexes, as well as the interpretation of the relevant results. D.M. calculated the ground-state magnetic anisotropy axes of the Dy^{III} centers in complex 3 and typed the manuscript. E.P. created the coordination polyhedra of the Ln^{III} atoms in the complexes. S.C. recorded the room-temperature, solid-state

electronic spectra of the complexes, and assigned the observed bands to the corresponding f-f transitions. P.D. collected single-crystal X-ray crystallographic data, solved the structures, performed their refinement, and wrote the relevant part of the paper. P.S.P., M.R. and R.C. performed the magnetic experiments, interpreted the results and wrote the relevant parts of the paper. P.D., R.C. and S.P.P. coordinated the research and wrote the final manuscript based on the reports of their collaborators. All authors exchanged opinions concerning the progress of the project and commented on the preparation of the manuscript at all stages. All authors have read and agreed to the published version of the manuscript.

Funding: D.M., E.P. and S.P.P. thank the MSc program “Analytical Chemistry and Nanotechnology” (Department of Chemistry, University of Patras, Patras, Greece) for providing funding for the purchase of few consumables, and the COST Action CA15128-Molecular Spintronics (MOLSPIN) for travel (to Bordeaux) funding and for encouraging research activities in Patras, Greece. P.D., M.R., P.P. and R.C. acknowledge the CNRS, University of Bordeaux, the Région Nouvelle Aquitaine, and the MOLSPIN COST action CA15128 and the GdR MCM-2 for support.

Acknowledgments: S.P.P. thanks Research Director Vassilis Psycharis for helpful discussions.

Conflicts of Interest: The authors declare no conflict of interest.

References

1. Cador, O.; Le Guennic, B.; Pointillart, F. Electro-activity and magnetic switching in lanthanide-based single-molecule magnets. *Inorg. Chem. Front.* **2019**, *6*, 3398–3417. [[CrossRef](#)]
2. Bagai, R.; Christou, G. The drosophila of single-molecule magnetism: $[Mn_{12}O_{12}(O_2CR)_{16}(H_2O)_4]$. *Chem. Soc. Rev.* **2009**, *38*, 1011–1026. [[CrossRef](#)]
3. Gatteschi, D.; Sessoli, R.; Villain, J. *Molecular Nanomagnets*; Oxford University Press: Oxford, UK, 2006.
4. Maniaki, D.; Pilichos, E.; Perlepes, S.P. Coordination Clusters of 3d-Metals That Behave as Single-Molecule Magnets (SMMs): Synthetic Routes and Strategies. *Front. Chem.* **2018**, *6*, 461. [[CrossRef](#)]
5. Ishikawa, N.; Sugita, M.; Ishikawa, T.; Koshihara, S.-Y.; Kaizu, Y. Lanthanide Double-Decker Complexes Functioning as Magnets at the Single-Molecular Level. *J. Am. Chem. Soc.* **2003**, *125*, 8694–8695. [[CrossRef](#)]
6. Briganti, M.; Fernandez Garcia, G.; Jung, J.; Sessoli, R.; Le Guennic, B.; Totti, F. Covalency and magnetic anisotropy in lanthanide single molecule magnets: The DyDOTA archetype. *Chem. Sci.* **2019**, *10*, 7233–7245. [[CrossRef](#)] [[PubMed](#)]
7. Canaj, A.B.; Singh, M.K.; Reginos Marti, E.; Damjanovic, M.; Wilson, C.; Céspedes, O.; Wernsdorfer, W.; Rajaraman, G.; Murrie, M. Boosting axiality in stable high-coordinate Dy(III) single-molecule magnets. *Chem. Commun.* **2019**, *55*, 5950–5953. [[CrossRef](#)] [[PubMed](#)]
8. Alexandropoulos, D.I.; Vinges, K.R.; Xie, H.; Dunbar, K.R. Switching On Single-Molecule Magnet Properties of Homoleptic Sandwich Tris(pyrazolyl)borate Dysprosium(III) Cations via Intermolecular Dipolar Coupling. *Dalton Trans.* **2019**, *48*, 10610–10618. [[CrossRef](#)]
9. Ortu, F.; Reta, D.; Ding, Y.-S.; Goodwin, C.A.P.; Gregson, M.P.; McInnes, E.J.L.; Winpenny, R.E.P.; Zheng, Y.-Z.; Liddle, S.T.; Mills, D.P.; et al. Studies of hysteresis and quantum tunneling of the magnetization in dysprosium(III) single molecule magnets. *Dalton Trans.* **2019**, *48*, 8541–8545. [[CrossRef](#)]
10. Hilgar, J.D.; Bernbeck, M.G.; Rinehart, J.D. Million-fold relaxation time enhancement across a series of phosphino-supported erbium single-molecule magnets. *J. Am. Chem. Soc.* **2019**, *141*, 1913–1917. [[CrossRef](#)]
11. Goodwin, C.A.P.; Reta, D.; Ortu, F.; Chilton, N.F.; Mills, D.P. Synthesis and Electronic Structures of Heavy Lanthanide Metallocenium Cations. *J. Am. Chem. Soc.* **2017**, *139*, 18714–18724. [[CrossRef](#)]
12. Guo, F.-S.; Day, B.M.; Chen, Y.-C.; Tong, M.-L.; Mansikkamäki, A.; Layfield, R.A. A Dysprosium Metallocene Single-Molecule Magnet Functioning at the Axial Limit. *Angew. Chem. Int. Ed.* **2017**, *56*, 11445–11449. [[CrossRef](#)]
13. Goodwin, C.A.P.; Ortu, F.; Reta, D.; Chilton, N.F.; Mills, D.P. Molecular magnetic hysteresis at 60 Kelvin in dysprosocenium. *Nature* **2017**, *548*, 439–442. [[CrossRef](#)] [[PubMed](#)]
14. Harriman, K.L.M.; Brosmer, J.L.; Ungur, L.; Diaconescu, P.L.; Murugesu, M. Pursuit of Record Breaking Energy Barriers: A Study of Magnetic Axiality in Diamide Ligated Dy^{III} Single-Molecule Magnets. *J. Am. Chem. Soc.* **2017**, *139*, 1420–1423. [[CrossRef](#)]
15. Gupta, S.K.; Rajeshkumar, T.; Rajaraman, G.; Murugavel, R. Is a strong axial crystal-field the only essential condition for a large magnetic anisotropy barrier? The case of non-Kramers Ho(III) versus Tb(III). *Dalton Trans.* **2018**, *47*, 357–366. [[CrossRef](#)] [[PubMed](#)]

16. Liu, J.; Chen, Y.-C.; Jia, J.-H.; Liu, J.-L.; Vieru, V.; Ungur, L.; Chibotaru, L.F.; Lan, Y.; Wernsdorfer, W.; Gao, S.; et al. A Stable Pentagonal-Bipyramidal Dy(III) Single-Ion Magnet with a Record Magnetization Reversal Barrier over 1000 K. *J. Am. Chem. Soc.* **2016**, *138*, 5441–5450. [[CrossRef](#)] [[PubMed](#)]
17. Zhang, H.; Nakanishi, R.; Katoh, K.; Breedlove, B.K.; Kitagawa, Y.; Yamashita, M. Low coordinated mononuclear erbium(III) single-molecule magnets with C_{3v} symmetry: A method by altering single-molecule magnet properties by incorporating hard and soft donors. *Dalton Trans.* **2018**, *47*, 302–305. [[CrossRef](#)]
18. Ungur, L.; Chibotaru, L.F. Strategies toward High-Temperature Lanthanide-Based Single-Molecule Magnets. *Inorg. Chem.* **2016**, *55*, 10043–10056. [[CrossRef](#)] [[PubMed](#)]
19. Harriman, K.L.M.; Errulat, D.; Murugesu, M. Magnetic Axiality: Design Principles from Molecules to Materials. *Trends Chem.* **2019**, *1*, 425–439. [[CrossRef](#)]
20. Liddle, S.T.; Van Slageren, J. Improving f-element single molecule magnets. *Chem. Soc. Rev.* **2015**, *44*, 6655–6669. [[CrossRef](#)] [[PubMed](#)]
21. Zhang, P.; Guo, Y.-N.; Tang, J. Recent advances in dysprosium-based single molecule magnets: Structural overview and synthetic strategies. *Coord. Chem. Rev.* **2013**, *257*, 1728–1763. [[CrossRef](#)]
22. Woodruff, D.N.; Winpenny, R.E.P.; Layfield, R.A. Lanthanide Single-Molecule Magnets. *Chem. Rev.* **2013**, *113*, 5110–5148. [[CrossRef](#)] [[PubMed](#)]
23. Gupta, S.K.; Murugavel, R. Enriching lanthanide single-ion magnetism through symmetry and axiality. *Chem. Commun.* **2018**, *54*, 3685–3696. [[CrossRef](#)]
24. Rinehart, J.D.; Long, J.R. Exploiting single-ion anisotropy in the design of f-element single-molecule magnets. *Chem. Sci.* **2011**, *2*, 2078–2085. [[CrossRef](#)]
25. Chilton, N.F.; Collison, D.; McInnes, E.J.L.; Winpenny, R.E.P.; Soncini, A. An electrostatic model for the determination of magnetic anisotropy in dysprosium complexes. *Nat. Commun.* **2013**, *4*, 2551–2557. [[CrossRef](#)] [[PubMed](#)]
26. Liu, J.-L.; Chen, Y.-C.; Tong, M.-L. Symmetry strategies for high performance lanthanide-based single-molecule magnets. *Chem. Soc. Rev.* **2018**, *47*, 2431–2453. [[CrossRef](#)] [[PubMed](#)]
27. Zhang, P.; Zhang, L.; Tang, J. Lanthanide single molecule magnets: Progress and perspective. *Dalton Trans.* **2015**, *44*, 3923–3929. [[CrossRef](#)] [[PubMed](#)]
28. Pointillart, F.; Cador, O.; Le Guennic, B.; Quahab, L. Uncommon lanthanide ions in purely 4f Single Molecule Magnets. *Coord. Chem. Rev.* **2017**, *346*, 150–175. [[CrossRef](#)]
29. Pedersen, K.S.; Woodruff, D.N.; Bendix, J.; Clérac, R. Experimental Aspects of Lanthanide Single-Molecule Magnet Physics. In *Lanthanides and Actinides in Molecular Magnetism*; Layfield, R.A., Murugesu, M., Eds.; Wiley-VCH: Weinheim, Germany, 2015; pp. 125–152.
30. Lada, Z.G.; Katsoulakou, E.; Perlepes, S.P. Synthesis and Chemistry of Single-molecule Magnets. In *Single-Molecule Magnets: Molecular Architectures and Building Blocks for Spintronics*; Holynska, M., Ed.; Wiley-VCH: Weinheim, Germany, 2019; pp. 245–313.
31. Rinehart, J.D.; Fang, M.; Evans, W.J.; Long, J.R. Strong exchange and magnetic blocking in N_2^{3-} -radical-bridged lanthanide complexes. *Nat. Chem.* **2011**, *3*, 538–542. [[CrossRef](#)] [[PubMed](#)]
32. Tang, J.; Zhang, P. Polynuclear Lanthanide Single Molecule Magnets. In *Lanthanides and Actinides in Molecular Magnetism*; Layfield, R.A., Murugesu, M., Eds.; Wiley-VCH: Weinheim, Germany, 2015; pp. 61–88.
33. Blagg, R.J.; Ungur, L.; Tuna, F.; Speak, J.; Comar, P.; Collison, D.; Wernsdorfer, W.; McInnes, E.J.L.; Chibotaru, L.F.; Winpenny, R.E.P. Magnetic relaxation pathways in lanthanide single-molecule magnets. *Nat. Chem.* **2013**, *5*, 673–678. [[CrossRef](#)] [[PubMed](#)]
34. Anwar, M.U.; Al-Harrasi, A.; Rawson, J.M.; Cavey, E.L.; Regier, J.; Alexandropoulos, D.; Pilkington, M.; Thompson, L.K. Slow magnetic relaxation in Dy_2 and Dy_4 complexes of a versatile, trifunctional polydentate N, O-ligand. *Dalton Trans.* **2019**, *48*, 14269–14278. [[CrossRef](#)]
35. Guo, F.-S.; Day, B.M.; Chen, Y.-C.; Tong, M.-L.; Mansikkamäki, A.; Layfield, R.A. Magnetic hysteresis up to 80 Kelvin in a dysprosium metallocene single-molecule magnet. *Science* **2018**, *362*, 1400–1403. [[CrossRef](#)] [[PubMed](#)]
36. Cotton, S.A. *Lanthanide and Actinide Chemistry*; Wiley: Chichester, UK, 2006.
37. Lucas, J.; Lucas, P.; LeMercier, T.; Rollat, A.; Davenport, W.G. *Rare Earths: Science, Technology, Production and Use*; Elsevier: Amsterdam, The Netherlands, 2014.

38. Gould, C.; Randall McClain, R.; Yu, J.; Groshens, T.J.; Furche, F.; Harvey, B.G.; Long, J.R. Synthesis and Magnetism of Neutral, Linear Metallocene Complexes of Terbium(III) and Dysprosium(III). *J. Am. Chem. Soc.* **2019**, *141*, 12967–12973. [[CrossRef](#)] [[PubMed](#)]
39. Habib, F.; Murugesu, M. Lessons learned from dinuclear lanthanide nano-magnets. *Chem. Soc. Rev.* **2013**, *42*, 3278–3288. [[CrossRef](#)] [[PubMed](#)]
40. Aromi, G.; Aguilà, D.; Gamez, P.; Luis, F.; Roubeau, O. Design of magnetic coordination complexes for quantum computing. *Chem. Soc. Rev.* **2012**, *41*, 537–546. [[CrossRef](#)]
41. Aguilà, D.; Barrios, L.A.; Velasco, V.; Roubeau, O.; Repollés, A.; Alonso, P.J.; Sesé, J.; Teat, S.J.; Luis, F.; Aromi, G. Heterodimetallic [LnLn'] Lanthanide Complexes: Toward a Chemical Design of Two-Qubit Molecular Spin Quantum Gates. *J. Am. Chem. Soc.* **2014**, *136*, 14215–14222. [[CrossRef](#)]
42. Aguilà, D.; Barrios, L.A.; Luis, F.; Repollés, A.; Roubeau, O.; Teat, S.J.; Aromi, G. Synthesis and Properties of a Family of Unsymmetric Dinuclear Complexes of Ln^{III} (Ln = Eu, Gd, Tb). *Inorg. Chem.* **2010**, *49*, 6784–6786. [[CrossRef](#)]
43. Jiang, Y.; Brunet, G.; Holmberg, R.J.; Habib, F.; Korobkov, I.; Murugesu, M. Terminal solvent effects of the anisotropy barriers of Dy₂ systems. *Dalton Trans.* **2016**, *45*, 16709–16715. [[CrossRef](#)]
44. Guo, Y.-N.; Xu, G.-F.; Wernsdorfer, W.; Ungur, L.; Guo, Y.; Tang, J.; Zhang, H.-J.; Chibotaru, L.F.; Powell, A.K. Strong Axiality and Ising Exchange Interaction Suppress Zero-Field Tunneling of Magnetization of an Asymmetric Dy₂ Single-Molecule Magnet. *J. Am. Chem. Soc.* **2011**, *133*, 11948–11951. [[CrossRef](#)]
45. Diaz-Ortega, I.F.; Herrera, J.M.; Aravena, D.; Ruiz, E.; Gupta, T.; Rajaraman, G.; Nojiri, H.; Colacio, E. Designing a Dy₂ Single-Molecule Magnet with Two Well-Differentiated Relaxation Processes by Using a Nonsymmetric Bis-bidentate Bipyrimidine-N-Oxide Ligand: A Comparison with Mononuclear Counterparts. *Inorg. Chem.* **2018**, *57*, 6362–6375. [[CrossRef](#)]
46. Aguilà, D.; Barrios, L.A.; Velasco, V.; Arnedo, L.; Aliaga-Alcalde, N.; Menelaou, M.; Teat, S.J.; Roubeau, O.; Luis, F.; Aromi, G. Lanthanide Contraction within a Series of Asymmetric Dinuclear [Ln₂] Complexes. *Chem. Eur. J.* **2013**, *19*, 5881–5891. [[CrossRef](#)]
47. Grove, H.; Kelly, T.L.; Thompson, L.K.; Zhao, L.; Xu, Z.; Abedin, T.S.M.; Miller, D.O.; Goeta, A.E.; Wilson, C.; Howard, J.A.K. Copper(II) Complexes of a Series of Alkoxy Diazine Ligands: Mononuclear, Dinuclear and Tetranuclear Examples with Structural, Magnetic and DFT Studies. *Inorg. Chem.* **2004**, *43*, 4278–4288. [[CrossRef](#)] [[PubMed](#)]
48. Pilichos, E.; Spanakis, E.; Maniaki, E.-K.; Raptopoulou, C.P.; Psycharis, V.; Turnbull, M.M.; Perlepes, S.P. Diversity of Coordination Modes in a Flexible Ditopic Ligand Containing 2-Pyridyl, Carbonyl and Hydrazone Functionalities: Mononuclear and Dinuclear Cobalt(II) Complexes, and Tetranuclear Copper(II) and Nickel(II) Clusters. *Magnetochemistry* **2019**, *5*, 39. [[CrossRef](#)]
49. Akkurt, M.; Khandar, A.A.; Tahir, M.N.; Yazdi, S.A.H.; Afkhami, F.A. Dibromido {N'-[1-(pyridin-2-yl)ethylidene]picolinohydrazide-κ²N',O} cadmium. *Acta Crystallogr. Sect. E Struct. Rep. Online* **2012**, *68*, m842. [[CrossRef](#)] [[PubMed](#)]
50. Xu, Z.-Q.; Mao, X.-J.; Zhang, X.; Cai, H.-X.; Bie, H.-Y.; Xu, J.; Jia, L. Syntheses, Crystal Structures and Antitumor Activities of Three Ln(III) Complexes with 2-Acetylpyridine Picolinohydrazone. *Chin. J. Inorg. Chem.* **2015**, *31*, 1–8.
51. Kitamura, F.; Sawaguchi, K.; Mori, A.; Takagi, S.; Suzuki, T.; Kobayashi, A.; Kato, M.; Nakajima, K. Coordination Structure Conversion of Hydrazone-Palladium(II) Complexes in the Solid State and in Solution. *Inorg. Chem.* **2015**, *54*, 8436–8448. [[CrossRef](#)]
52. Mahmoudi, G.; Bauzá, A.; Gurbanov, A.V.; Zubkov, F.I.; Maniukiewicz, W.; Rodriguez-Dieguez, A.; López-Torres, E.; Frontera, A. The role of unconventional stacking interactions in the supramolecular assemblies of Hg(II) coordination compounds. *CrystEngComm* **2016**, *18*, 9056–9066. [[CrossRef](#)]
53. Mahmoudi, G.; Stilinovic, V.; Bauzá, A.; Frontera, A.; Bartyzel, A.; Ruiz-Pérez, C.; Kirillov, A.M. Inorganic-organic hybrid materials based on PbBr₂ and pyridine-hydrazone blocks-Structural and theoretical study. *RSC Adv.* **2016**, *6*, 60385–60393. [[CrossRef](#)]
54. Dawe, L.N.; Abedin, T.S.M.; Kelly, T.K.; Thompson, L.K.; Miller, D.O.; Zhao, L.; Wilson, C.; Leech, M.A.; Howard, J.A.K. Self-assembled polymetallic square grids ([2×2] M₄, [3×3] M₉) and trigonal bipyramidal clusters (M₅)-structural and magnetic properties. *J. Mater. Chem.* **2016**, *16*, 2645–2659. [[CrossRef](#)]

55. Abedi, M.; Yesilel, O.Z.; Mahmoudi, G.; Bauzá, A.; Lofland, S.E.; Yerli, Y.; Kaminsky, W.; Garczarek, P.; Zareba, I.K.; Ienco, A.; et al. Tetranuclear Manganese(II) Complexes of Hydrazone and Carboxyhydrazone Ligands: Synthesis, Crystal Structures, Magnetic Properties, Hirshfeld Surface Analysis and DFT Calculations. *Inorg. Chim. Acta* **2016**, *443*, 101–109. [[CrossRef](#)]
56. Coxall, R.A.; Harris, S.G.; Henderson, D.K.; Parsons, S.; Tasker, P.A.; Winpenny, R.E.P. Inter-ligand reactions: In situ formation of new polydentate ligands. *J. Chem. Soc. Dalton Trans.* **2000**, 2349–2356. [[CrossRef](#)]
57. Mylonas-Margaritis, I.; Mayans, J.; Sakellakou, S.-M.; Raptopoulou, C.P.; Psycharis, V.; Escuer, A.; Perlepes, S.P. Using the Singly Deprotonated Triethanolamine to Prepare Dinuclear Lanthanide(III) Complexes: Synthesis, Structural Characterization and Magnetic Studies. *Magnetochemistry* **2017**, *3*, 5. [[CrossRef](#)]
58. Anastasiadis, N.C.; Granadeiro, C.M.; Mayans, J.; Raptopoulou, C.P.; Bekiari, V.; Cunha-Silva, L.; Psycharis, V.; Escuer, A.; Balula, S.S.; Konidaris, K.F.; et al. Multifunctionality in Two Families of Dinuclear Lanthanide(III) Complexes with a Tridentate Schiff-Base Ligand. *Inorg. Chem.* **2019**, *58*, 9581–9585. [[CrossRef](#)] [[PubMed](#)]
59. Anastasiadis, N.C.; Kalofolias, D.A.; Philippidis, A.; Tzani, S.; Raptopoulou, C.P.; Psycharis, V.; Milios, C.J.; Escuer, A.; Perlepes, S.P. A family of dinuclear lanthanide(III) complexes from the use of a tridentate Schiff base. *Dalton Trans.* **2015**, *4*, 10200–10209. [[CrossRef](#)] [[PubMed](#)]
60. Anastasiadis, N.C.; Mylonas-Margaritis, I.; Psycharis, V.; Raptopoulou, C.P.; Kalofolias, D.A.; Milios, C.J.; Klouras, N.; Perlepes, S.P. Dinuclear, tetrakis(acetato)-bridged lanthanide(III) complexes from the use of 2-acetylpyridine hydrazone. *Inorg. Chem. Commun.* **2015**, *51*, 99–102. [[CrossRef](#)]
61. Nikolaou, H.; Terzis, A.; Raptopoulou, C.P.; Psycharis, V.; Bekiari, V.; Perlepes, S.P. Unique Dinuclear, Tetrakis(nitrato-O,O')-Bridged Lanthanide(III) Complexes from the Use of Pyridine-2-Amidoxime: Synthesis, Structural Studies and Spectroscopic Characterization. *J. Surf. Interfaces Mater.* **2014**, *2*, 311–318. [[CrossRef](#)]
62. Anastasiadis, N.C.; Granadeiro, C.M.; Klouras, N.; Cunha-Silva, L.; Raptopoulou, C.P.; Psycharis, V.; Bekiari, V.; Balula, S.S.; Escuer, A.; Perlepes, S.P. Dinuclear Lanthanide(III) Complexes by Metal-Ion-Assisted Hydration of Di-2-pyridyl ketone Azine. *Inorg. Chem.* **2013**, *52*, 4145–4147. [[CrossRef](#)]
63. Bekiari, V.; Thiakou, K.A.; Raptopoulou, C.P.; Perlepes, S.P.; Lianos, P. Structure and photophysical behavior of 2,2-bipyrimidine/lanthanide ion complexes in various environments. *J. Lumin.* **2008**, *128*, 481–488. [[CrossRef](#)]
64. Messimeri, A.; Papadimitriou, C.; Raptopoulou, C.P.; Escuer, A.; Perlepes, S.P.; Boudalis, A.K. The benzoate/nitrate/2,2':6',2''-terpyridine 'blend' in lanthanide(III) chemistry. Relevance to the separation of lanthanides and actinides by solvent extraction. *Inorg. Chem. Commun.* **2007**, *10*, 800–804. [[CrossRef](#)]
65. Thiakou, K.A.; Nastopoulos, V.; Terzis, A.; Raptopoulou, C.P.; Perlepes, S.P. Di-2-pyridyl ketone in lanthanide(III) chemistry: Mononuclear and dinuclear erbium(III) complexes. *Polyhedron* **2006**, *25*, 539–549. [[CrossRef](#)]
66. Thiakou, K.A.; Bekiari, V.; Raptopoulou, C.P.; Psycharis, V.; Lianos, P.; Perlepes, S.P. Dinuclear lanthanide(III) complexes from the use of di-2-pyridyl ketone: Preparation, structural characterization and spectroscopic studies. *Polyhedron* **2006**, *25*, 2869–2879. [[CrossRef](#)]
67. Pilichos, E.; Mylonas-Margaritis, I.; Kontos, A.P.; Psycharis, V.; Klouras, N.; Raptopoulou, C.P.; Perlepes, S.P. Coordination and metal ion-mediated transformation of a polydentate ligand containing oxime, hydrazine and picolinoyl functionalities. *Inorg. Chem. Commun.* **2018**, *94*, 48–52. [[CrossRef](#)]
68. Nakamoto, K. *Infrared and Raman Spectra of Inorganic and Coordination Compounds*, 4th ed.; Wiley: New York, NY, USA, 1986; pp. 254–257.
69. Maniaki, D.; Mylonas-Margaritis, I.; Mayans, J.; Savvidou, A.; Raptopoulou, C.P.; Bekiari, V.; Psycharis, V.; Escuer, A.; Perlepes, S.P. Slow magnetic relaxation and luminescence properties in lanthanide(III)/anil complexes. *Dalton Trans.* **2018**, *47*, 11859–11872. [[CrossRef](#)] [[PubMed](#)]
70. Carnall, W.T.; Fields, P.R.; Kajnak, K. Electronic Energy Levels in the Trivalent Lanthanide Aquo Ions. I. Pr^{3+} , Nd^{3+} , Pm^{3+} , Sm^{3+} , Dy^{3+} , Ho^{3+} , Er^{3+} , and Tm^{3+} . *J. Chem. Phys.* **1968**, *49*, 4424–4442. [[CrossRef](#)]
71. Carnall, W.T.; Fields, P.R.; Rajnak, K. Electronic Energy Levels of the Trivalent Lanthanide Aquo Ions. III. Tb^{3+} . *J. Chem. Phys.* **1968**, *49*, 4447–4449. [[CrossRef](#)]
72. Karraker, D.G. The Hypersensitive Transitions of Nd^{3+} , Ho^{3+} and Er^{3+} Ions. *Inorg. Chem.* **1968**, *7*, 473–479. [[CrossRef](#)]
73. Karraker, D.G. Hypersensitive Transitions of Six-, Seven-, and Eight-Coordinate Neodymium, Holmium, and Erbium Chelates. *Inorg. Chem.* **1967**, *6*, 1863–1868. [[CrossRef](#)]

74. Llunell, M.; Casanova, D.; Girera, J.; Alemany, P.; Alvarez, S. *SHAPE, Continuous Shape Measures Calculation; Version 2.0*; Universitat de Barcelona: Barcelona, Spain, 2010.
75. Long, J.; Habib, F.; Lin, P.-H.; Korobkov, I.; Enright, G.; Ungur, L.; Wernsdorfer, W.; Chibotaru, L.F.; Murugesu, M. Single-Molecule Magnet Behavior for an Antiferromagnetically Superexchange-Coupled Dinuclear Dysprosium(III) Complex. *J. Am. Chem. Soc.* **2011**, *133*, 5319–5328. [[CrossRef](#)]
76. Roy, L.E.; Hughbanks, T. Magnetic Coupling in Dinuclear Gd Complexes. *J. Am. Chem. Soc.* **2006**, *128*, 568–575. [[CrossRef](#)]
77. Lecren, L.; Wernsdorfer, W.; Li, Y.-G.; Roubeau, O.; Miyasaka, H.; Clérac, R. Quantum Tunneling and Quantum Phase Interference in a $[\text{Mn}^{\text{II}}_2\text{Mn}^{\text{III}}_2]$ Single-Molecule Magnet. *J. Am. Chem. Soc.* **2005**, *127*, 11311–11317. [[CrossRef](#)]
78. Van Vleck, I.H. Paramagnetic Relaxation Times for Titanium and Chrome Alum. *Phys. Rev.* **1940**, *57*, 426–447. [[CrossRef](#)]
79. Mazarakioti, E.C.; Regier, J.; Cunha-Silva, L.; Wernsdorfer, W.; Pilkington, M.; Tang, J.; Stamatatos, T.C. Large Energy Barrier and Magnetization Hysteresis at 5 K for a Symmetric $\{\text{Dy}_2\}$ Complex with Spherical Tricapped Trigonal Prismatic Dy^{III} ions. *Inorg. Chem.* **2017**, *56*, 3568–3578. [[CrossRef](#)] [[PubMed](#)]
80. Cole, K.S.; Cole, R.H. Dispersion and Absorption in Dielectrics I. Alternating Current Characteristics. *J. Chem. Phys.* **1941**, *9*, 341–351. [[CrossRef](#)]
81. Reta, D.; Chilton, N.F. Uncertainty estimates for magnetic relaxation times and magnetic relaxation parameters. *Phys. Chem. Chem. Phys.* **2019**, *21*, 23567–23575. [[CrossRef](#)]
82. Shrivastava, K.N. Theory of Spin–Lattice Relaxation. *Phys. Stat. Sol. A* **1983**, *117*, 437–458. [[CrossRef](#)]
83. Abragam, A.; Bleaney, B. *Electron Paramagnetic Resonance of Transition Ions*; Dover: New York, NY, USA, 1986.
84. Ding, M.; Hickey, A.K.; Pink, M.; Telser, J.; Tierney, D.L.; Amoza, M.; Rouzières, M.; Ozumzerzifon, T.J.; Hoffert, W.A.; Shores, M.P.; et al. Magnetization Slow Dynamics in Ferrocenium Complexes. *Chem. Eur. J.* **2019**, *25*, 10625–10632. [[CrossRef](#)] [[PubMed](#)]
85. Pescia, J. La relaxation des spins électronique avec le réseau. *J. Phys.* **1966**, *27*, 782–800. [[CrossRef](#)]
86. Sheldrick, G.M. *SADABS Version 2.03*; Bruker Analytical X-Ray Systems: Madison, WI, USA, 2000.
87. Sheldrick, G.M. Crystal structure refinement with SHELXL. *Acta Crystallogr. Sect. C* **2015**, *71*, 3–8. [[CrossRef](#)] [[PubMed](#)]

Sample Availability: Samples of the compounds 1–4 are available from the authors.



© 2020 by the authors. Licensee MDPI, Basel, Switzerland. This article is an open access article distributed under the terms and conditions of the Creative Commons Attribution (CC BY) license (<http://creativecommons.org/licenses/by/4.0/>).